Earth, Planets and Space

FULL PAPER Open Access

MIRS: an imaging spectrometer for the MMX mission

Maria Antonietta Barucci[1*], Jean-Michel Reess[1], Pernelle Bernardi[1], Alain Doressoundiram[1], Sonia Fornasier[1], Michel Le Du[2], Takahiro Iwata[3], Hiromu Nakagawa[4], Tomoki Nakamura[4], Yves André[2], Shohei Aoki[3], Takehiko Arai[6], Elisa Baldit[2], Pierre Beck[7], Jean-Tristan Buey[1], Elisabet Canalias[2], Matthieu Castelnau[2], Sebastien Charnoz[8], Marc Chaussidon[8], Fréderic Chapron[1], Valerie Ciarletti[9], Marco Delbo[10], Bruno Dubois[11], Stephane Gauffre[12], Thomas Gautier[9], Hidenori Genda[13], Rafik Hassen-Khodja[9], Gilles Hervet[2], Ryuki Hyodo[3], Christian Imbert[2], Takeshi Imamura[14], Laurent Jorda[15], Shingo Kameda[16], Driss Kouach[11], Toru Kouyama[17], Takeshi Kuroda[4], Hiroyuki Kurokawa[13], Laurent Lapaw[9], Jeremie Lasue[18], Laetitia Le Deit[19], Aurélien Ledot[2], Cedric Leyrat[1], Bertrand Le Ruyet[1], Moe Matsuoka[1], Frederic Merlin[1], Hideaki Miyamoto[14], Frederic Moynier[8], Napoleon Nguyen Tuong[1], Kazunori Ogohara[20], Takahito Osawa[21], Jérôme Parisot[1], Laurie Pistre[2], Benjamin Quertier[12], Sean N. Raymond[12], Francis Rocard[5], Takeshi Sakanoi[4], Takao M. Sato[22], Eric Sawyer[2], Fériel Tache[1], Sylvain Trémolières[2], Fuminori Tsuchiya[4], Pierre Vernazza[23] and Didier Zeganadin[1]

Abstract

The MMX infrared spectrometer (MIRS) is an imaging spectrometer onboard MMX JAXA mission. MMX (Martian Moon eXploration) is scheduled to be launched in 2024 with sample return to Earth in 2029. MIRS is built at LESIA-Paris Observatory in collaboration with four other French laboratories, collaboration and financial support of CNES and close collaboration with JAXA and MELCO. The instrument is designed to fully accomplish MMX's scientific and measurement objectives. MIRS will remotely provide near-infrared spectral maps of Phobos and Deimos containing compositional diagnostic spectral features that will be used to analyze the surface composition and to support the sampling site selection. MIRS will also study Mars atmosphere, in particular spatial and temporal changes such as clouds, dust and water vapor.

Keywords: MIRS, MMX, Imaging spectrometer, Phobos, Deimos, Mars

*Correspondence: antonella.barucci@obspm.fr
[1] LESIA-Observatoire de Paris, Université PSL, CNRS, Sorbonne Université, Université de Paris, 5 place Jules Janssen, 92195 Meudon, France
Full list of author information is available at the end of the article

Graphical Abstract

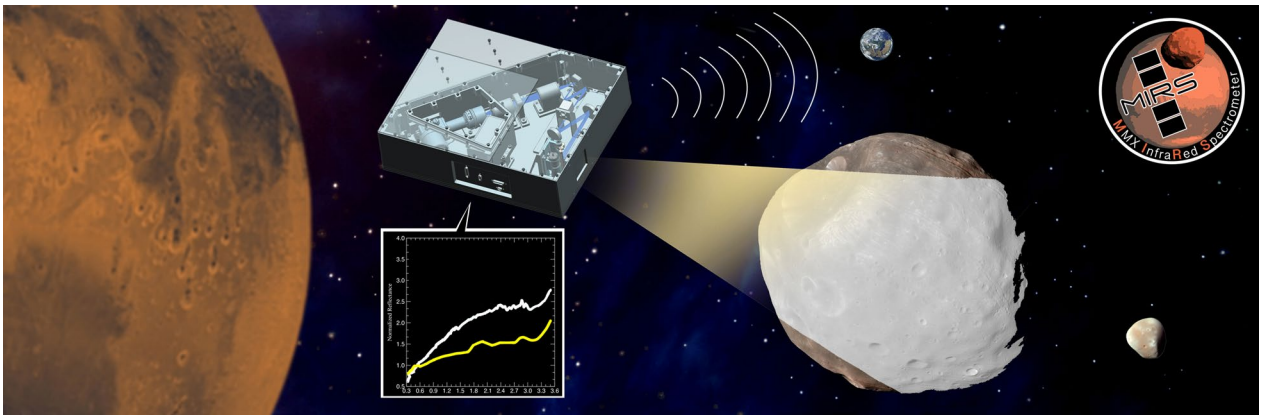

Introduction

MIRS (MMX InfraRed Spectrometer) is an imaging spectrometer working from 0.9 to 3.6 μm with spectral resolution better than 20 nm. MIRS will work during the 3 years of the MMX stay in circum-Martian space (Kuramoto et al. 2021). The imaging spectrometer will provide global spectral characterization of Phobos and Deimos to map the surface composition, to support the Phobos sampling site selection and give detailed surface composition of the two sampling sites. MIRS will also study Mars atmosphere with particular attention to local time variation on the spatial distribution of water vapor, dust, clouds, and other atmospheric species, which could not be traced by previous satellites on the sun-synchronous polar orbit.

MIRS will contribute to the two major goals (Kuramoto et al. 2021) of the MMX mission:

1. Clarify the origins of the Martian moons and constrain processes for planetary formation and material transport in the region connecting the inner and outer solar system
2. Clarify the driving mechanism of the transition of the Mars–moons system and add new knowledge to the evolution history of Mars.

Controversy on the origin of the Martian moons

The origin of Phobos and Deimos is a debated question and attacking this problem represents the major MMX mission goal. Remote sensing observations by Viking 1 and 2, Mariner 9 and Phobos-2 revealed that the heavily cratered surface, the mass and the low density of Phobos and Deimos shared similarities with asteroids. In addition, as detailed in the following sections, their spectra are very different from those of the martian surface, being red sloped (i.e., reflectance increases with wavelength), without strong absorption features and resembling the spectra of primitive C- and D-type asteroids.

Following the aforesaid observations, it was suggested that Phobos and Deimos could be captured asteroids. Asteroidal capture by a planet is possible if a dissipative process is at play to extract orbital energy from the passing body. This requires either that the object is braked in a circumplanetary atmosphere (Sasaki 1990), or in 3-body encounters where a binary asteroid is split by tides, and one body remains trapped in planetocentric orbit, and the others escape the planet (Hansen et al. 2018), or if tidal dissipation is intense enough (Kaula 1964). However, none of these processes can easily explain the close-to-zero inclination of Phobos and Deimos (with respect to Mars' equatorial plane). Indeed objects coming from the Asteroid belt may encounter Mars with high inclinations (Mars obliquity varies between 10° and 40° (Laskar and Robutel 1993; Touma and Wisdom 1993). Captured objects may remain on high eccentricity and high inclinations orbits with respect to the planet. Whereas tides may damp orbital inclination and eccentricity of a captured Phobos in less than 4.6 Gyrs (Burns 1992), owing to its larger size and closer distance to Mars, they are much less efficient for the case of Deimos that orbits beyond 6 Martian radii (Szeto 1983; Burns 1992).

An alternative explanation for the formation of a Martian disk was fostered by Craddock (2011) who suggested that an impact onto Mars may have formed a circumplanetary disk, and that Phobos and Deimos accreted locally from disk material. Reaccumulation

of disk material into rubble piles naturally leads to the formation of a collection of a dozen of moons (Rosenblatt and Charnoz 2012; Rosenblatt et al. 2016; Canup and Salmon 2018) with masses between those of Deimos and up to 1000 times Phobos. Most moons would be tidally driven inward over time and impacts on the planet. In this view (Rosenblatt et al. 2016), Phobos would be the last surviving moon of this old population, whereas Deimos would be the only moon that accreted beyond Mars' synchronous orbit, and have experienced only little dynamical evolution.

Recently, Hesselbrock and Minton (2017) suggested that Phobos suffers multiple cycle of tidal destruction and re-accretion close to Mars' Roche limit (about 3 Mars radii), implying potentially that the today Phobos may have accreted only recently (< 100 Myrs).

In the giant impact hypothesis, Phobos and Deimos would be made of a mix (50–50%) of Martian mantle and impactor material (the origin of which is unconstrained). The temperatures that were reached during the impact are just high enough to melt silicate minerals, in the range of 2000 K only (Hyodo et al. 2017). However, this would be enough to devolatilize material and the resulting composition could resemble devolatilized Martian mantle with maybe substantial signs of oxidation if the impactor was water rich (Hyodo et al. 2018; Pignatale et al. 2018).

Regardless of the origin of Martian moons, exogenic materials from the natural meteoroid impact and Martian materials ejected by small impacts on Mars would be mixed in the regolith of Phobos and Deimos (Ramsley and Head 2013; Hyodo et al. 2019), whereas, these late accreted masses are of the order of ~ 1000–10,000 ppm fraction in their regolith (Hyodo et al. 2019) and thus the change in the bulk surface composition would be negligible. If Phobos is formed by a giant impact, Phobos should contain high-temperature phase materials representing a mixture of Martian silicates (from crust and mantle).

MIRS will be able to characterize the global composition of Phobos and Deimos surface material (and subsurface through the mapping of crater ejectas) and will be able to support the selection of the two Phobos sampling sites. In combination with the sample return from Phobos, MIRS data will help deciphering whether Phobos composition is closer to that of C-D type asteroids (with similarity to carbonaceous chondrites and presence of organics or ices), which would imply a capture origin, or is more similar to a devolatilized and/or hydrated Martian mantle. This latter case would indicate, at the same time, a giant impact origin for Phobos and Deimos and would also give clues to the characteristics of the putative impactor onto Mars (see paper by Nakamura et al. 2021).

MIRS scientific objectives

MIRS is expected to characterize Phobos and Deimos surfaces and Mars atmospheric composition by remotely identifying diagnostic features in the near-infrared spectral range.

MIRS is used to achieve several of the mission requirements (MR), in particular:

MR.1: To grasp the surface distribution of the constituent materials of Phobos. Hydrous minerals and other related minerals should be identified and characterized spectroscopically for main parts of the full body in correspondence with its topography (at horizontal spatial resolutions of 20 m or better) and in a radius of 50 m or more around the sampling point (at spatial resolutions of 1 m or better).
MR.2: To grasp the distribution of constituent materials of Deimos, from spectroscopic information. Clarify the surface distribution of hydrous minerals and other related minerals corresponding to its topography for some characteristic areas of the moon's surface with a horizontal spatial resolution of 100 m or better.
MR.3: To constrain transport processes of dust and water near the Martian surface, continuous observations of the mid- to low-latitude distributions of dust storms, ice clouds, and water vapor in the Martian atmosphere will be performed from high-altitude equatorial orbit in different seasons to within 1-h time resolutions.

Phobos

Due to the proximity of Phobos and Deimos to Mars, accurate analyses were possible only with the arrival of space missions (Mariner and Viking orbiters). The first images of Phobos from Mariner 7 allowed the estimation of the size and of the albedo of the satellite, found to be the darkest object known in the Solar System at that time (Smith 1970). Later measurements confirmed the low albedo of Phobos ($7.1 \pm 1.2\%$, Simonelli et al. 1998). Higher-resolution imaging from Viking 1 and 2 revealed the complex surface geomorphology of Phobos, characterized by km-long grooves, craters in a variety of degradation states with variable diameter up to the larger 9.4-km-sized Stickney crater (Thomas et al. 1979).

Several spectra of Phobos were acquired by Mariner 9, Viking 1 and 2 confirming that it is a dark body with featureless spectra in the visible–UV range comparable to low-albedo asteroids (Pang et al. 1978; Pollack et al. 1978). Thanks to the Phobos-2 mission, spatially resolved spectra were acquired with the imaging spectrometer for Mars (ISM), revealing heterogeneity in reflectance and

spectral properties across Phobos surface at spatial resolution of 0.7–1 km (Bibring et al. 1989, 1992). Two spectral units were identified, the 'red unit' occupying most of the surface, and the 'blue unit' associated with Stickney crater. The two units differ mainly on spectral slope and brightness, the red one having a higher spectral slope, and the bluer one being brighter and with a lower slope (Murchie et al. 1991; Murchie and Erard 1996). Blue unit is associated with fresher areas close to the Stickney crater and initially considered as fresh ejecta deposit. However, high resolution images from HiRISE instrument on Mars Reconnaissance Orbiter (MRO) revealed that blue unit is seen both inside and outside the crater rim, and that within it several underlying spots of the red unit are present (Thomas et al. 2011), indicating that Phobos has a heterogeneous composition made of blocks of red and blue units (Basilevsky et al. 2014).

No clear absorption bands were detected from Phobos-2 data, and spectra acquired from ground-based telescopes observations indicate no 3 μm absorption feature due to hydrated minerals with an upper limit of 5–10% (Fig. 1 from Rivkin et al. 2002).

The featureless red-sloped low-albedo spectra of Phobos, coupled with its low density (1860 ± 13 kg m^{-3}, Willner et al. 2014), were associated with primitive outer-belt/outer Solar System bodies, such as the D-type asteroids, Jupiter Trojans, ultrared transneptunians (Rivkin et al. 2002).

Further high-resolution spectra were acquired by the CRISM and OMEGA spectrometers, respectively, onboard MRO and Mars Express missions (Fig. 1). These instruments acquired high signal-to-noise ratio (SNR) spectra revealing spectral features in both Phobos units (Fig. 1), at a spatial resolution of about 350 m/pixel (Fraeman et al. 2014). The red unit of Phobos and also Deimos show a weak 0.65 μm absorption feature consistent with desiccated Fe-phyllosilicate such as nontronite (Murchie et al. 2008; Fraeman et al. 2014). An alternative interpretation of this feature includes anhydrous silicates and space weathering effects producing micro- and nanophase iron which acts as Rayleigh scatters generating the 0.65 μm feature (Clark et al. 2012). This feature on Phobos was confirmed from ground-based observations covering the red unit (Murchie et al. 2015), by Pathfinder data (Simonelli et al. 1998), and by ROSETTA mission observations with its OSIRIS cameras (Pajola et al. 2013).

CRISM also detected a sharp absorption at 2.8 μm in both units of Phobos, and on Deimos, with depth varying from 1 to 10% (Fraeman et al. 2014). Note that CRISM data in the 2.70–2.76 μm wavelength range were compromised by a boundary between filters mounted to the IR detector that blocks higher orders from the diffraction grating; these wavelengths were not routinely downlinked by the instrument. This feature is stronger on Deimos and Phobos red unit, and weaker on Phobos' bluer unit. An absorption feature in the 3-μm region was observed on several asteroids, and it is typically caused by a combination of the very strong OH-radical absorption feature and the first overtone of the 6-μm H_2O fundamental (Rivkin et al. 2002). Adsorbed water has a symmetric stretch, giving rise to an absorption feature at 3.1 μm, and an antisymmetric stretch feature at 2.9 μm.

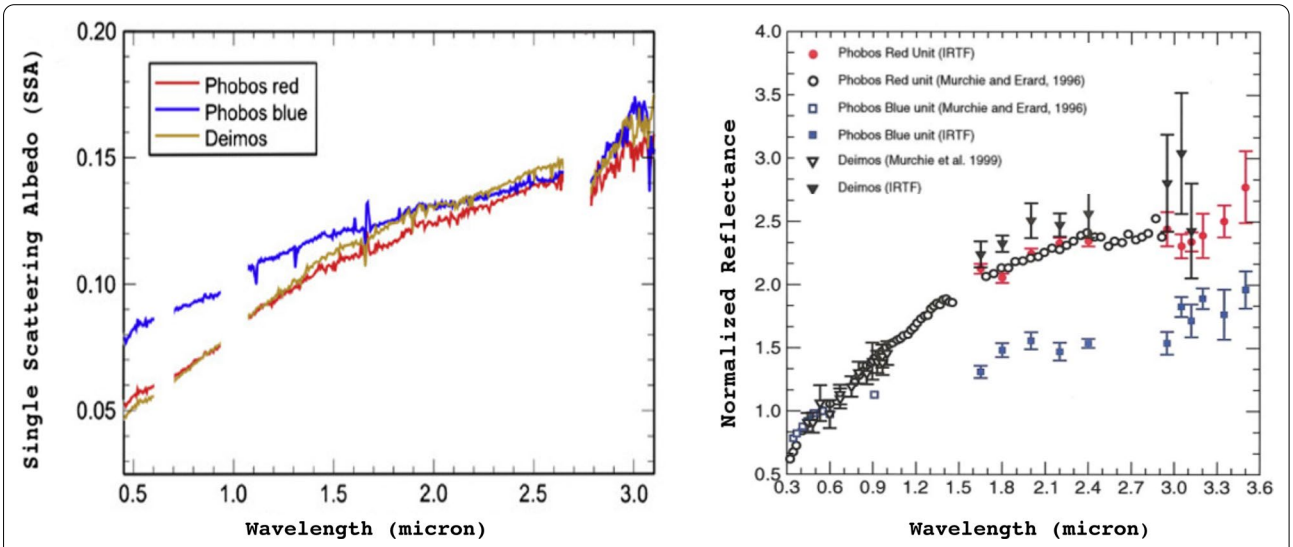

Fig. 1 Left: single scattering albedo spectra (SSA) for the Phobos blue and red units, and for Deimos, derived from CRISM-MRO spectra, extracted from Fraeman et al. (2014). Right: combination of several spectra covering the 0.3–3.6 μm range of Phobos and Deimos, extracted from Rivkin et al. (2002)

Structural hydroxyl (OH) that has been incorporated into mineral lattices produces a stretch absorption at 2.7 μm. The depth of the fundamental H_2O/OH feature depends on many parameters besides abundance of hydrated material, including particle size, albedo, and temperature. In the case of Mars satellites, the strength, position, and shape of the 2.8 μm band is attributed to OH, and there is no clear evidence of absorptions in the 3–3.1 micron region due to adsorbed water or water ice (Rivkin et al. 2002; Fraeman et al. 2014).

No other diagnostic absorptions appear in the VIS–NIR range in either Phobos or Deimos spectra, in particular any related to common ferrous minerals (olivine, pyroxene). The red slope and the absorption bands detected in the visible and NIR region are consistent with those of hydrated asteroids interpreted to have primitive composition (C-, G-, P-, and D-class asteroids, Fraeman et al. 2014). The emissivity spectra of Phobos derived by TES data suggest an ultramafic composition with the presence of phyllosilicates and feldspathoids in some regions (Giuranna et al. 2011). Recently, Glotch et al. (2015) from MIR data, suggest the presence of bound molecular water and carbonate on the surface of Phobos. This result needs confirmation, but these aforementioned observations seem to point to a spectral analogy between the Mars moons and primordial asteroids, thus favoring the asteroid capture hypothesis.

Deimos

The first data of Deimos were also acquired by Mariner 9 and Viking orbiters, suggesting that Deimos was spectrally similar to C-type objects (summarized by Burns 1992), an idea that was challenged by Grundy and Fink (1992) who found much steeper spectral slopes for this body that were inconsistent with carbonaceous chondrites and more consistent with reddish D-type asteroid. As indicated in the previous section and shown in Fig. 1, Deimos shares similar spectral properties with Phobos red unit, in terms of high spectral slope, and it shows the same faint features at 0.65 μm and 2.8 μm, possibly indicating a composition rich in desiccated phyllosilicates.

Rivkin et al. (2002) observed Deimos using the IRTF and combined several spectra obtained from the literature to generate a complete spectrum from 0.3 to 3.6 μm (Fig. 1). While there is strong caveat in the whole near-infrared range and that the spectral resolution of the data is usually low, they confirm, from their analyses, the anhydrous nature of the surface of Deimos, placing limits on the 3-μm band depth at roughly 10–20%. They also state that spectral analogs for the Martian satellites are difficult to find in the asteroid belt, and it seems that the outer-belt D asteroids have spectra which bracket spectral pattern of Deimos.

The Viking data suggested the trailing side is about 10% brighter than the leading side. This leads us to assume a modest difference in materials composition or properties on the two sides of Deimos. This is consistent with the successive Hubble Space Telescope data that also showed slight leading/trailing differences on Deimos (Zellner and Wells 1994). Differences exist in the visible albedo and are correlated with topography rather than found in more coherent units as on Phobos (Thomas et al. 1996). High spatial resolution color observations of Deimos were not obtained by Phobos-2, and the Viking data which exist are in a very restricted wavelength range. The Imager for Mars Pathfinder (IMP) obtained disk-integrated, visible-range spectrophotometric data for the sub-Mars hemispheres of Deimos (Murchie et al. 1999), showing Deimos is quite homogeneously red, consistent with the results of Grundy and Fink (1992).

Although there may be small differences in the material properties of Phobos and Deimos, the drastic visual difference most probably derives from the smoothing effects of the large impact that formed the 10-km wide southern polar depression on Deimos (Thomas et al. 1996). This impact is relatively much larger than the Stickney impact crater on Phobos. Thus some previous suggestions that the lack of grooves on Deimos stemmed from a lack of large craters (Thomas et al. 1979) need revision, either in the fracture origin of grooves or on the timing of ejecta re-accretion covering the effects of fracturing. Extend these analyses in the near-infrared spectral range is fundamental in order to explore the possible spatial variation of the chemical composition of Deimos and answer the still open questions.

MIRS in the exploration of the Phobos and Deimos surface

Fraeman et al. (2014) proposed two hypotheses to explain the spectral features on Phobos and Deimos. The first invokes the presence of highly desiccated Fe-phyllosilicate minerals inherent to Phobos and Deimos, consistent with the presence of primordial material in the Moons' formation region, and the second appeals exogenic processes associated with the solar wind which may have created Fe and OH on the moons' surface. However, there are no telescopic- or space-based data sets with sufficient spectral range and SNR levels to independently validate this feature's presence. OMEGA observations of Phobos do cover the necessary wavelength range, but a detector boundary with an unknown offset near 2.7 μm makes it impractical to detect a weak absorption. Observations of Phobos and Deimos with MIRS will allow to check the presence of this absorption feature and its variation on the whole Phobos and Deimos surfaces, and possibly discard one of these hypotheses described by Fraeman et al. (2014) by characterizing the 2.7-μm absorption

band features (i.e., band peak position and shape; Donaldson et al. 2016, and Pieters et al. 2009, for instance). At further extent, detection of phyllosilicates would imply that the origin of Phobos from a Giant impact is less likely. Yet, a global assessment of composition is needed to identify and evaluate the properties and geologic context of different materials. As presented in Pieters et al. (2014), diverse materials are known to exist across the surface of Mars moons and it is essential to document their characteristics, distribution, and the spatial relationships between them. MIRS will be on front seat to fulfill this goal.

MIRS will observe Phobos and Deimos in the 0.9–3.6 μm range with a spectral resolution better than 20 nm. For Phobos, MIRS will acquire spectra at SNR > 100 and at a spatial resolution of about 20 m (for ± 30° latitude) during the QSO-M (quasi-satellite orbit—medium altitude, see Table 3) global survey. A higher spatial resolution of 1 m will be reached over an area within 50 m from the selected sampling sites. The spectral radiometric absolute accuracy is expected to be of 10%, and the relative accuracy of 1%. The high SNR and unprecedented spatial resolution achieved by MIRS will permit to fully characterize the composition and mineralogy of both the red and blue units on Phobos and further investigate the local compositional heterogeneity associated with the different geomorphological features across Phobos surface. The capability of MIRS fulfills completely mission requirements for Phobos. It will also possibly provide new insights into space weathering processes thanks to resolved spectral observations of small fresh craters.

MIRS is expected to spectroscopically detect and characterize, if any, water (ice) (absorption bands at 1.5, 2.0 and 3.0–3.2 μm), hydrous silicate minerals (features at 2.7–2.8 μm, and minor overtones at 1.4 and 1.8 μm), or anhydrous silicates (bands in the 0.9–1 and 2.0 μm regions). If possible, also to measure organic matter (3.3–3.5 μm). Thanks to high SNR, it will also allow a detailed characterization of the absorption bands detected, permitting by the precise investigation of the band center, depth and area to well constrain the mineralogy, species abundances and composition of Phobos. These unprecedented data will allow scientists to cast light on the origin of Mars moons.

For Deimos, MIRS is expected to spectroscopically map major regions at a spatial resolution better than 100 m and at SNR better than 100 below 3.2 μm in less than 2 s, and detect the same major absorption bands as observed in Phobos. Such observational conditions will allow us to spatially probe the surface of Deimos and constrain the surface composition as well as search more efficiently possible weak spectral features (a full characterization of the bands is possible for band depth as weak as 3%, estimated from a Monte Carlo approach, and based on synthetic spectra reaching SNR of about 100), as in the case of Phobos. The data will also favor the search for physical and chemical heterogeneity that could be linked to topography or linked to the Martian phase aspect. Do the particle size or the chemical content of the leading and trailing sides are different, as suspected from the observation performed with HST in the visible range? The lack of current data of Deimos, especially in terms of spatially resolved spectral data, considerably reduce our ability to constrain the surface properties of it, and even if Deimos is not the target for the sampling, we will clearly be able to take advantage of this mission to considerably improve the physical and chemical knowledge of the surface of this satellite, and bring new insights about the history of the Martian environment.

Temperature on Phobos and Deimos

Temperature is a fundamental physical parameter that affects a number of physical processes important for remote sensing of planetary surfaces, including the reflected and emitted radiance. On solar system bodies the temperature is primarily determined by the heliocentric distance, its time derivative and by variations in the illumination caused by the cycles between day and night and seasons. In addition, on atmosphere-less bodies, such as Phobos and Deimos, temperatures are also controlled by the physical properties of their surfaces, the most important one being the albedo, the roughness, the heat capacity, the density, and the thermal conductivity of the surface. The latter is function of the porosity of the material and grain size in the case of regolith. When illumination conditions vary periodically and thermal conductivity is independent of depth, it is possible to define the thermal inertia as the square root of the product of thermal conductivity, density, and heat capacity, and show that surface temperatures are governed by the value of the thermal inertia (e.g., Spencer et al. 1989). When its value is lower than some hundreds J m^{-2} $s^{-1/2}$ K^{-1} at heliocentric distances of few AU, temperatures can vary dramatically between winter and summer and between day and night (e.g., Delbo et al. 2015).

The latter is the case of the surfaces of Phobos and Deimos that express temperatures ranging between ~ 50 K and ~ 300 K (Kührt and Giese 1989). These large temperature variations are in part due to the low value of the thermal conductivity (Gatley et al. 1974) or thermal inertia (Lunine et al. 1982; Kührt et al. 1992). The large temperature variations are also caused by the complex orbital geometry of these satellites, including their synchronous rotations with their orbital periods, the eclipses they are subject to, and the seasons. In the case of Phobos, which

orbits Mars at an altitude of only ~ 6000 km from the surface of red planet, the reflected scattered light and thermal emission from Mars are also important in determining the surface temperature of the satellite (Kührt and Giese 1989). The low albedo of these satellites and its variations across the surface, with values ranging between 0.05 and 0.10 in the visible band (Fraeman et al. 2014), also contribute to temperature differences.

It is known that temperature can affect the near-infrared spectral features (e.g., Singer and Roush 1985; Roush and Singer 1987; Lucey et al. 1998; Moroz et al. 2000). For instance, at low temperature, the visible and near-infrared bands narrow and the band contrast increases compared to their measurements at higher temperatures. The change in the spectral band properties is related to the composition of the surface and the grain size of dust potentially covering it. It is therefore conceivable that spectral observations of the martian moons' surfaces at different temperatures (e.g., different time of the day) will help constraining their composition.

By means of computer codes that implement the so-called thermal (or thermophysical) models (e.g., Delbo et al. 2015 for a review) we calculate model temperatures, or the corresponding emitted infrared radiance as a function of physical parameters such as the albedo, roughness, and thermal inertia, which are adjusted until best match between the model predictions and the observations are obtained, thereby constraining the physical properties of the surface (Delbo et al. 2015). Modeling of surface temperatures will be essential to estimate the heat and radiation environment for near surface operations of MMX, which is important to support the sampling sites selection and operations.

On the other hand, the physical parameters estimated from the analysis of the infrared observations will be interpreted in terms of grain sizes of the surface regolith (e.g., Gundlach and Blum 2013; Sakatani et al. 2017; Ryan et al. 2020) or porosity of surface rocks (as in Grott et al. 2019), using radiative transfer models. This will contribute to provide geologic context of Phobos returned samples. Thermal inertia (or conductivity) values have been derived for Phobos by several authors using measurements from different space missions and also from ground-based data: Gatley et al. (1974) found thermal conductivity values that would correspond to a thermal inertia < 15 J m^{-2} $s^{-1/2}$ K^{-1} using Mariner 9 radiometric data, while Lunine et al. (1982) obtained a range of thermal inertia values between 40 and 70 J m^{-2} $s^{-1/2}$ K^{-1} from Viking data, and Kührt et al. (1992) determined thermal inertia values between 20 and 40 J m^{-2} $s^{-1/2}$ K^{-1}. All these values are quite low and would imply that the surface is made of a fine-grained particulate material (regolith). Kührt and Giese (1989) proposed that thermal properties dependent on temperatures must be used on Phobos and Deimos. Bandfield et al. (2018) found that the best effective thermal inertia value is 150 J m^{-2} $s^{-1/2}$ K^{-1}, a value that they claim to be still compatible with particulate regolith. The same authors also reported a more successful model fit where thermal inertia varies with depth, from 50 at the surface to 1000 J m^{-2} $s^{-1/2}$ K^{-1} in the shallow subsurface. Smith et al. (2019) derived the first disk resolved map of the thermal inertia of some regions of Phobos. They found a mean thermal inertia value of 42 J m^{-2} $s^{-1/2}$ K^{-1} with a range of values between 20 and 100 J m^{-2} $s^{-1/2}$ K^{-1}.

MIRS will measure the spectral radiance of the surface within the instrument footprint (Fig. 2). This is essentially the reflected solar spectrum with superimposed minerals absorption bands. At wavelengths longer than about 2.5 μm the so-called thermal tail kicks due to Phobos thermal radiation become more important than the reflected sun-light. The thermal tail is a strong function of the temperature and thus MIRS data can be used to derive the surface temperature as long as the latter is high enough to produce a radiance signal above the instrument sensitivity. The thermal tail is also function of the infrared emissivity. Modeling the thermal tail is an important aspect of the MIRS data analysis, in particular in the region around 2.7–2.8 μm where the reflectance spectra will be investigated for the presence of the phyllosilicate and water bands.

Despite MIRS is not a proper thermal instrument due to its limited wavelength extension in the infrared, the thermal tail can be used to assess the surface temperature and its spatial and temporal variations. From temperature measurements, information about the surface thermal inertia of Phobos will be derived. This has been done at similar wavelengths with the OSIRIS-REx Visible and InfraRed Spectrometer (OVIRS; Reuter et al. 2018) onboard NASA's OSIRIS-REx asteroid sample return missions (Lauretta et al. 2015) to successfully determine the thermal inertia of the surface of the asteroid Bennu with spatial resolutions of some meters (DellaGiustina et al. 2019).

Mars

Mars atmosphere

Mars atmosphere is strongly coupled to the surface. This is especially the case regarding volatiles species in strong interaction with the polar caps. This effect, together with seasonal variation of the radiative balance, induces a high seasonality in the volume mixing ratio of species such as H_2O, CO or O_2. The suspended dust particles from the surface contribute to localized heating of the atmosphere and have a significant impact on the global climatology on Mars, especially during the dust storm seasons. All of these atmospheric components (Table 1) present

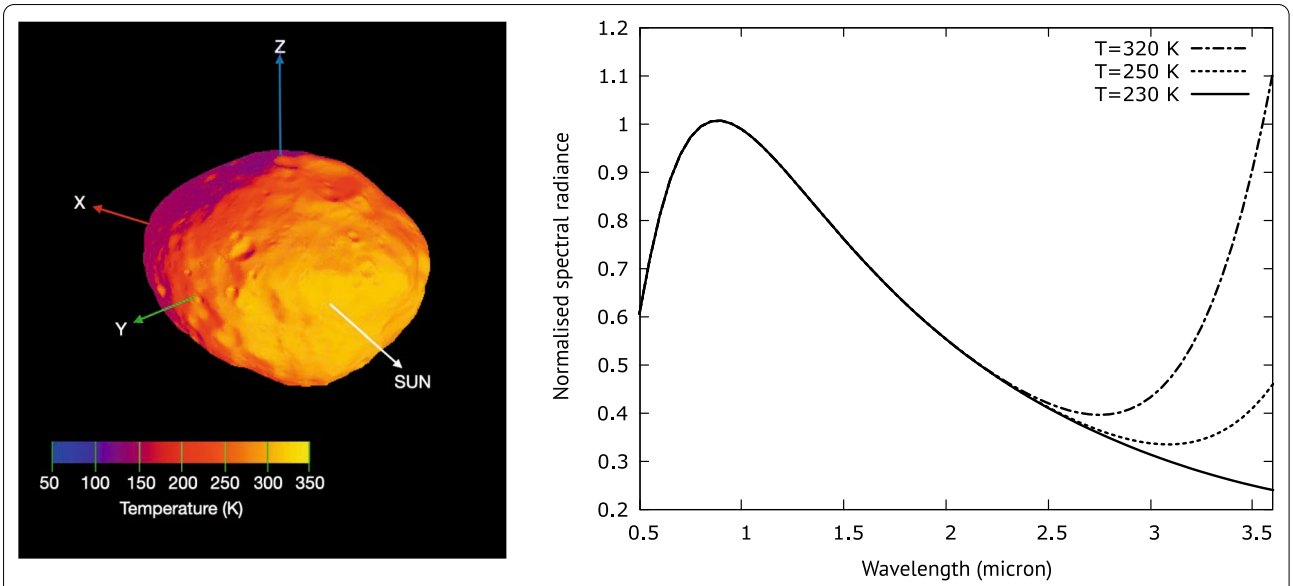

Fig. 2 Left: preliminary temperature calculation on Phobos using the Gaskell shape model (Gaskell 2011). The model was reduced to 98,000 facets to speed-up calculations. Temperatures decrease from yellow to red to blue. Right: spectral radiance calculated using the thermal model and assuming that the reflected light component is a reddened solar spectrum. The spectral radiance is normalized to 1 at the peak of the curve. Notice the strong thermal tail that arises in MIRS relevant wavelengths and its strong dependence on temperature

Table 1 Main targets of the Mars science measured by MIRS

Target	Parameters	Spectral range
Ice cloud formation and evolution	Water ice clouds	1.5, 2 and 3-μm bands
Dust clouds/storms formation and evolution	Dust	CO_2 2.7-μm band or 0.9–3.6 μm
Water cycle	H_2O	2.6-μm band
Atmospheric composition and dynamics	Surface pressure	CO_2 2.0-μm band
	CO	2.3-μm band
Limb observations for middle atmosphere	O_2 dayglow (water index)	1.27-μm band

significant signatures in the MIRS spectral range, from 0.9 to 3.6 μm (see Fig. 3).

While being the main Martian atmospheric component, CO_2 presents a strong seasonal cycle due to its condensation at the polar caps, which induces strong fluctuation of Martian surface pressure. On top of that, small oscillations of the surface pressure, which are key diagnostic to meteorological events, were observed by OMEGA onboard Mars Express (Forget et al. 2007; Spiga et al. 2007). MIRS will have the capability to monitor CO_2 and thus pressure through inversion of its 2.0 μm band as it was performed with the OMEGA data. While the large-scale annual variation of water vapor has been stable for more than 20 Martian years (Montmessin et al. 2017), questions remain on the interaction between water vapor, ice clouds and dust on regional scales. The spatial resolution of MIRS for Mars observations (< 10 km) will extend the existing records on these observations and better constrain the interdependencies between these major atmospheric components. It is noteworthy that the MIRS measurements provide the first opportunity for investigating the diurnal variation and the transport processes of water vapor with time-resolved pictures of the atmospheric phenomena from the equatorial orbit.

Most of the information about water vapor on Mars has been obtained for more than two decades from MAWD onboard Viking 1 and 2, TES onboard Mars Global Surveyor, SPICAM, OMEGA, and PFS onboard Mars Express, CRISM onboard MRO missions (e.g., see review for SPICAM in Montmessin et al. 2017). These observations revealed a global cycle of water vapor, which is mainly driven by dynamics and sublimation–condensation process between the atmosphere and the polar caps, with a column integrated abundance peaking up to 40 pr-μm during northern summer in the polar region. On the other hand, local events such

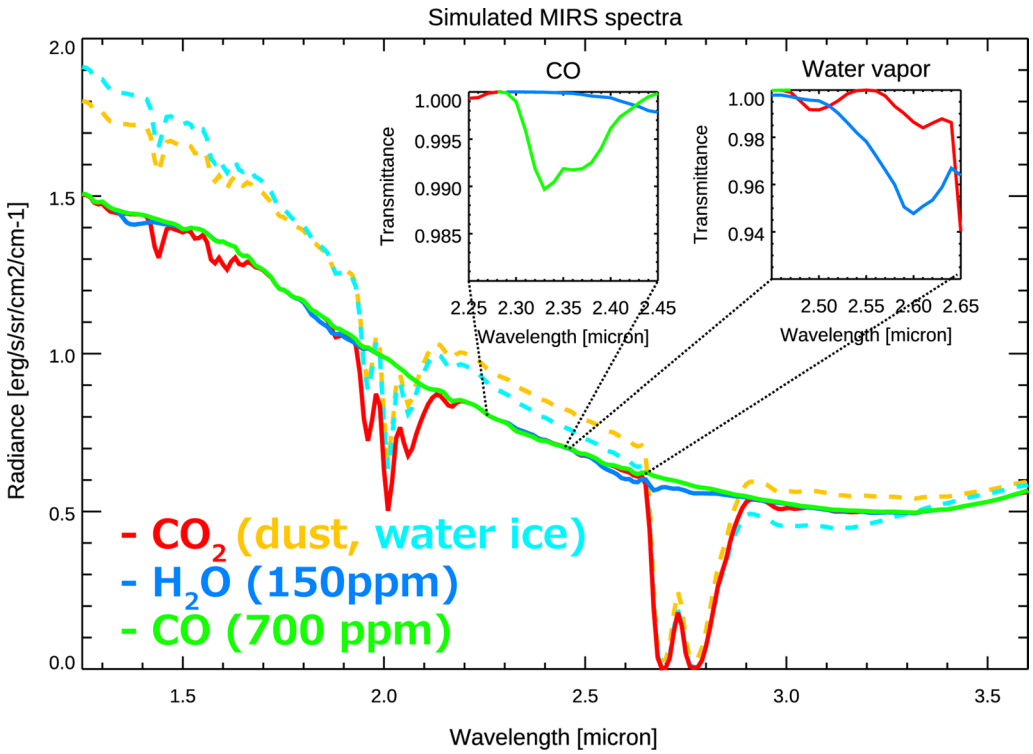

Fig. 3 Expected features of the Mars atmosphere observed by MIRS. The synthetic spectra are calculated by the widely used DISORT-based radiative transfer model for Mars (Ignatiev et al. 2005). A typical condition of Mars atmosphere is assumed. The surface albedo of Mars is assumed to be 0.15 (uniform). The thick curves in the figure show the spectra for the clear sky condition, and the dashed curves include the effects of dust or water ice clouds. For gases, CO_2, CO, and water vapor are calculated separately (red, orange, and blue curves, respectively). The calculated synthetic spectra are convolved with the instrumental line shape of MIRS that is a Gaussian function whose FWHM is 20 nm. The sampling step is 10 nm

as surface–atmosphere interaction and water vapor transport due to so-called rocket dust storm, that can lift dust rapidly and efficiently to high altitude (Spiga et al. 2013), are not well understood. Characterization of such local events requires high-frequency monitoring of water vapor with different local times. MIRS will have the first capability to monitor water vapor at low- to mid-latitude on a daily basis using its 2.6 μm band (Maltagliati et al. 2008). The adsorbed water in the regolith also can be monitored by the 3.0 μm band (Audouard et al. 2014). Water ice clouds also present large seasonal variations and spatial distribution, associated with both the water cycle and general atmospheric circulation (Montmessin et al. 2004). The most predominant ice clouds formation is found in a belt around the equator during Mars' aphelion season. These clouds are due to the release of large amount of water from the northern polar cap during spring and summer: this induces an increase in water vapor content at mid- to low-latitude where it can be uplifted by the Hadley circulation and this uplifting brings air charged in water to higher altitudes where low temperatures and pressures favor cloud condensation, allowing the seasonal persistence of this so-called Aphelion cloud belt. Water ice clouds can also be found at higher latitude during winters over polar caps (Fedorova et al. 2006; Montmessin et al. 2017; Vincendon et al. 2011). Water ice clouds will be identified primarily through their spectral features between 0.9 and 3.6 μm (Olsen et al. 2017). In addition to the water ice clouds, MIRS may be able to investigate the mesospheric CO_2 ice clouds. Recent observations have revealed the presence of the CO_2 ice clouds at remarkably high altitudes (above 40 km; mesosphere) (e.g., Montmessin et al. 2006; Aoki et al. 2018). However, the formation process of these peculiar clouds has not been measured even though it has been suggested that the clouds form in supersaturated pockets of air created by the interference of thermal tides and gravity waves (e.g., Clancy and Sandor 1998; Spiga et al. 2012). Its monitoring in the morning or evening will provide a first insight on its formation process. Vincendon et al. (2011) proposed a procedure to process CRISM observations to discriminate H_2O and CO_2 ice clouds by combining its visible images and near-infrared spectra and demonstrated its usefulness by comparing it with previous observations. This

procedure will be tentatively applied to coordinate MIRS and OROCHI observations to investigate mesospheric CO_2 ice clouds.

The relatively long lifetime of CO has a capability to trace the atmospheric dynamics on Mars. Its detection and quantification thus would allow for further refinement of current atmospheric dynamical models (e.g., Daerden et al. 2019). CO presents only a weak band at 2.3–2.4 μm within MIRS wavelength range. However, previous observation with OMEGA and CRISM, both instruments having similar SNR as MIRS, demonstrated the detectability of this compound. In addition, while the formation of CO is intrinsically linked to the CO_2 cycle, its non-condensation during polar winter, contrary to CO_2, induces a relative enrichment at mid- to high-latitudes. While we expect global detection of CO, the equatorial orbit of the MMX mission will make Hellas Planitia, where clear seasonal variations due to CO_2 condensation during southern winter have been evidenced by OMEGA and CRISM, our prime target for CO monitoring (Encrenaz et al. 2006; Smith et al. 2009).

O_2 is an oxidant tracer for atmospheric photochemistry on Mars. During the diurnal variation, it is formed through ozone UV photodissociation in the lower atmosphere (Fedorova et al. 2006). This induces a dayglow at 1.27 μm whose mapping thus provides a tracer for O_3 and its variations. O_2 dayglow shows its maxima during early spring at high latitudes, while low latitudes show a maximum at aphelion due to a peak in ozone concentration related to lower abundances of hydrogen radicals (Lefèvre et al. 2004). At high latitudes, O_2 can also be produced by CO_2 photodissociation, as it can be observed on the nightside at high latitudes via recombination of O brought in a downwelling general atmospheric circulation on the dayside in the upper atmosphere (Bertaux et al. 2012). This nightglow emission is a unique tracer for downward advection transport mechanism to constrain the mesospheric dynamics. The dayglow of O_2 formed via O_3 dissociation will be detectable with the MIRS instrument in nadir observations but also measurable at limb, which will provide its vertical profiles as well as an index of water vapor vertical profiles (Clancy et al. 2017). The nightglow would require limb observations at high latitudes that could technically be doable by MIRS, but may be extremely challenging to perform given MMX equatorial orbit. Another possible tentative measurement within the MIRS wavelength range would be the one of OH Meinel bands at 1.45 and 2.9 μm as detected by the CRISM instrument (Clancy et al. 2013). However, the detection of these extremely faint bands would require the accumulation of observations of the polar night limb and thus be subjected to the same limitation as the O_2 nightglow observations. As such, and while these two observations will be tentative, they are not considered a prime target for the MIRS instrument.

Mars surface and dust

Although the specifications of the MIRS imaging spectrometer are quite similar to previous instruments, such as OMEGA aboard MEX, the orbit of MMX can offer some advantages for global mapping of the red planet. The expected geometric resolution is ~ 2 km at the footprint on Mars surface, so a spatial binning can be possible to increase the SNR and save data volume. Being placed on the same orbit as Phobos around Mars, at about 6000 km of altitude, the spacecraft will have a ~ 7 h orbit around the planet, allowing to complete a global mapping of the surface of Mars within a few days. In addition, the well-controlled scanner system enables the specific pointing of the instrument, thus allowing MIRS measurements to obtain wide spatial coverage in hourly time-scale. Both these observing modes will be very useful to follow the temporal evolution of the atmospheric aerosols with a meso-scale spatial resolution. In that respect, MIRS will complement adequately the instruments that are already observing the Martian surface and atmosphere from orbit. Its coverage will be more similar to that obtained with the MEX/OMEGA instrument, with the interesting capability to analyze the same area at high temporal resolution (5 times every 30 min), or to obtain almost global mapping of the sunlit hemisphere with 5 h of observations. This capability will allow to survey rapidly changing atmospheric events. Based on the similarities with previous observations, existing techniques that have already been applied to analyze the spectral cubes from the atmosphere of Mars with previous missions can be also applied to the MIRS data and improved.

The analysis of the spectra taken on the slopes of large volcanoes, such as the Olympus Mons can help to probe different atmosphere thicknesses and detect the column density of H_2O, CO_2 and dust constituents in the Martian atmosphere (Combes et al. 1991; Rosenqvist et al. 1992). To go further into the analysis of the different atmospheric constituents, Mars limb observations should allow to directly recover at first order the spectral signature of aerosols present in the atmosphere though it will depend on the properties and composition of the aerosols at different altitudes (Erard et al. 1994). Furthermore, limb observations by MIRS have a capability to investigate the vertical structure of aerosols in a global view. It is interesting to note that high-altitude (above 60 km) H_2O was first identified by SPICAM occultation (Maltagliati et al. 2011, 2013) especially in the southern summer, which happens to be a dusty season. They reported the links between such high-altitude H_2O and aerosols in their vertical profiles within a short time-scale. This implies

the importance of aerosols for key processes in the Martian water cycle and climate as a whole. MIRS will provide further information of the new pathway of water loss proposed by recent studies (Chaffin et al. 2017; Heavens et al. 2018).

A better estimate of the reflectance spectrum from the light backscattered by atmospheric aerosols can be obtained by comparing the successive observations of identical zones on the surface of Mars within a short time and with varying phase angles. Such a set of measurements permits to decorrelate the surface reflectance signal from the light scattered by the aerosols suspended in the atmosphere of Mars and gives information on the aerosols size and composition properties. Such an analysis for the ISM data (on-board Phobos-2 spacecraft) taken over Tharsis and Ophir Planum showed that the spectra thus obtained are consistent with a particle size distribution having an effective radius of 1.2 ± 0.2 μm (Erard et al. 1994). Features of the spectrum indicate the presence of water ice, and possible absorption due to clays and/or sulfates. The overall parameters that can be obtained from such an analysis include the scattering albedo, the phase function of the aerosols, the optical thickness, τ, of the atmosphere and the aerosols size distribution with possible indications on their shape.

Vincendon et al. (2007, 2009) have shown that the introduction of a radiative transfer model can improve on the first estimates for these values, which was demonstrated as an application to the OMEGA data. It was also possible during Martian dust storms to obtain typical properties of the Martian suspended dust in terms of scattering albedo and optical depth by applying independent components multivariate methods to separate the spectrum signal of the aerosols from the one from the surface and the atmospheric gas (Määttänen et al. 2009). An improvement of the method used to correct for aerosols light scattering by multi-angle analysis over 11 different viewing geometries to retrieve the Mars surface photometric properties was developed for CRISM by including non-isotropic surface materials reflectance (Ceamanos et al. 2013; Fernando et al. 2013). Further CRISM observations of the limb of Mars allowed to retrieve locations and properties of the aerosols on the atmosphere of Mars (Smith et al. 2013). To go further, combined observations of CRISM limb observations, MCS and MARCI were used to determine the composition and sizes of Mars mesospheric aerosols and ice clouds dynamics (Clancy et al. 2019).

Finally, the combination with lander infrared measurements can allow to confirm and better constrain the local properties of atmospheric dust from the ground (Ockert-Bell et al. 1997). Assuming that Mars rovers are still active on the surface of the planet during the mission, it can be envisioned to combine the orbital measurements with those that will be made locally by using the infrared channel of the SuperCam instrument on Mars, for example (Maurice et al. 2021; Wiens et al. 2021) and the MastCam-Z multispectral camera observations (Bell et al. 2021). All these studies will improve our understanding of the optical properties of the Martian aerosols, their evolution with time and the exchanges between the surface and the atmosphere of the planet. In the end, understanding fully the contribution of aerosols to the measured reflectance from orbit will enable an improved understanding of the scattering properties of the Martian surface.

MIRS instrument

Push-broom spectrometer

MIRS is a spectrometer that uses the well-known push-broom acquisition principle (Fig. 4). A single detector acquisition (2D matrix) provides the image of a strip in one direction (spatial), and the spectrum of each point of the strip in the second direction (spectral). The second spatial dimension results from the motion of MIRS Line of Sight in the along-track direction either thanks to the spacecraft speed or by actuation of MIRS scanner.

The start of each image acquisition has to be adjusted so that:

- All images are as contiguous as possible: no overlaps, no holes.
- Integration time is sufficient to guarantee the required SNR, and short enough not to degrade the spatial resolution.

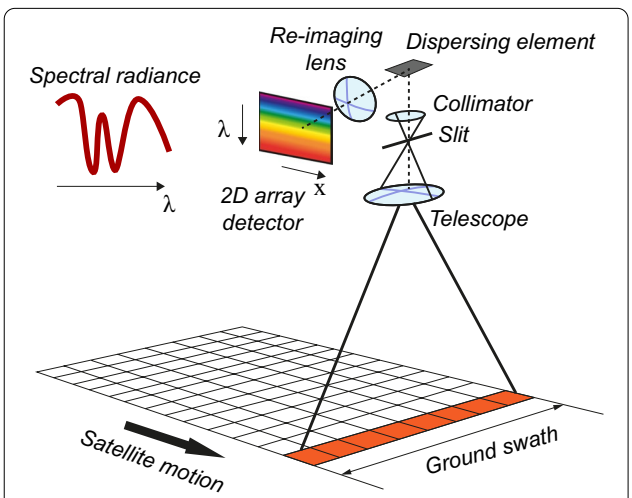

Fig. 4 Scheme for a push-broom spectrometer

We define the subsatellite point as the projection of MMX—Z axis on the celestial body of interest. Subsatellite ground speed varies and might not be adapted to MIRS acquisition principle. For Phobos observation on low-altitude trajectories, ground speed can be too high to ensure sufficient integration time between 2 images. However, for Phobos observation during descent phases, ground speed is nearly null. For Mars observation, ground speed is low enough to cover large zones.

In order to adjust ground speed of MIRS Line of Sight projection on celestial body of interest to these situations, MIRS is equipped with an along-track scanner with $\pm 20°$ optical amplitude. This scanner can also be used to perform observations of zones with specific phase angle and local solar time by commanding a constant along-track bias. Meanwhile, the cross-track latitudes can be reached using the spacecraft maneuvers.

Instrument concept

MIRS is an infrared imaging spectrometer (Fig. 5). Based on scientific objectives, the MIRS technical requirements have been derived as presented in Table 2. The spectral dispersion is obtained with a low-density groove grating working in order 1. The telescope is composed of two free form mirrors (highly aspherical mirrors) focusing the scene target on the entrance slit of the spectrometer. The collimator is also composed of two free form mirrors projecting the entrance slit at infinity. The grating is located at the pupil of the instrument. Then two dioptric objectives are used. The first one projects the spectral image on a filter that sorts the grating orders. The second one projects this spectral image on the detector, but also images the pupil on a cold stop in order to limit the background flux due to the thermal emission of the spectrometer. The detector and the cold stop are encapsulated in a cryostat and cooled down to 110 K (120 K for the cold stop).

A shutter is placed in the slit plane in order to close the spectrometer cavity after the telescope and acquire background images that can be subtracted to science data.

A cover is positioned at the entrance of the instrument to limit dust pollution when landing on Phobos.

MIRS is mounted on the exploration module (Fig. 6) and is connected to the MDP for data management (TC/TM and image compression) and the PDCU for power supply (Fig. 7).

MIRS consists of three subunits:

– An Optical Box (OBOX) (Fig. 8A, B) containing all the optical components (Fig. 8C): mechanisms (scanner, shutter, dust cover), a telescope, a spectrometer, a calibration source, and a detector package with

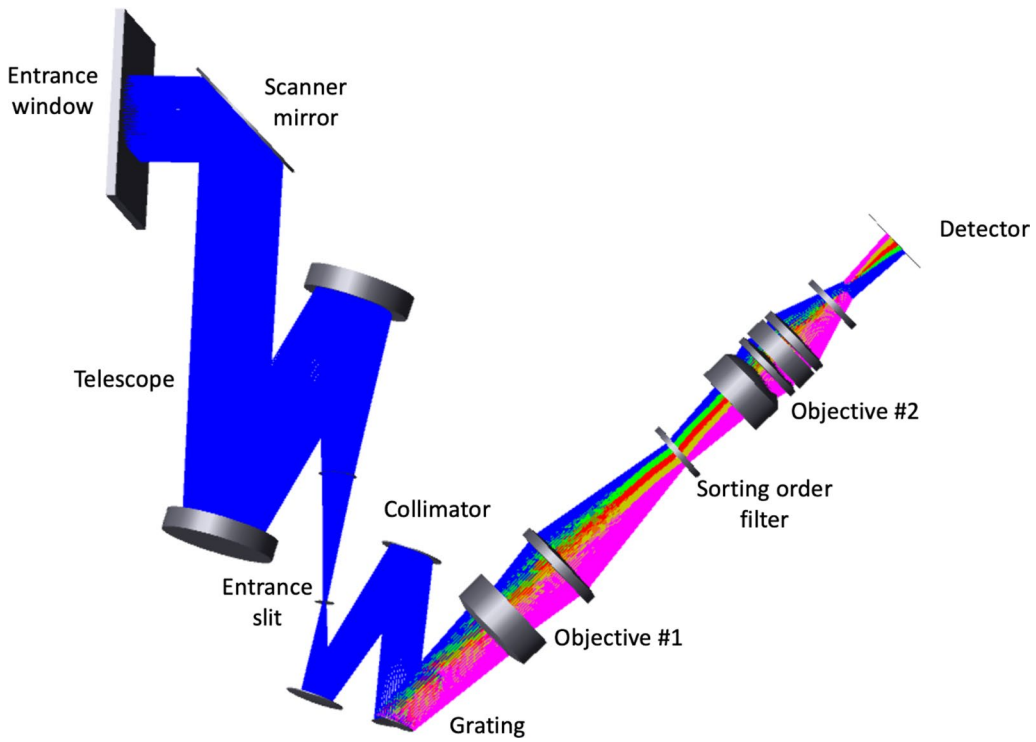

Fig. 5 MIRS optical design overview

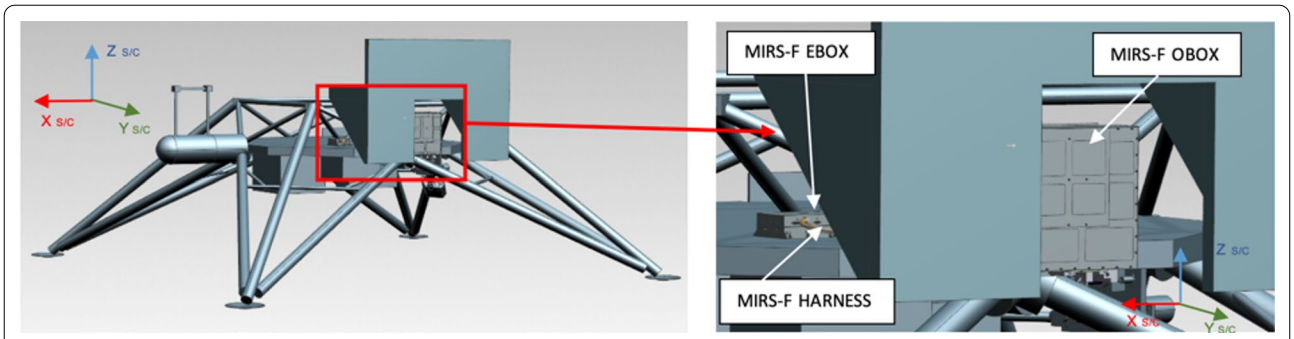

Fig. 6 MIRS on MMX exploration module

Table 2 MIRS performance requirements

Requirement ID	Requirement
MIRS-PE-001	Spectral range: 0.9–3.6 µm
MIRS-PE-002	Spectral resolution (sampled) < 20 (+ 10%) nm
MIRS-PE-003	Spectral sampling: 10 (+ 10%) nm
MIRS-PE-004	IFOV: ≤ 0.41 mrad, goal: 0.35 mrad
MIRS-PE-005	FOV: ≥ ± 1.65°
MIRS-PE-006	SNR: ≥ 100 in [2.7—3.2] µm in less than 2 s integration, for 30° solar incidence, at 1.5 au, with Lambertian albedo at 30° phase angle
MIRS-PE-007	Modulation transfer function shall be higher than 8% at Nyquist frequency in the spatial direction
MIRS-PE-008	MIRS boresight orientation with respect to MMX spacecraft shall be known with an accuracy better than ± 1.4 mrad
MIRS-PE-009	MIRS boresight relative orientation between successive acquisitions of an observation sequence shall be known with an accuracy better than ± 0.17 mrad Note: an observation sequence is: A complete observation run when the scanner is not used (e.g., Phobos global mapping) The observation phase corresponding to a scan when the scanner is continuously rotating during images acquisition (e.g., Mars, Phobos landing)
MIRS-PE-010	Spectral registration: knowledge better than 5 nm
MIRS-PE-011	Absolute radiometric calibration: better than 10%
MIRS-PE-012	Relative radiometric calibration: better than 1%
MIRS-PE-013	Distortion (spatial): knowledge better than 0.5 pixel. Goal 0.2 pixel

its dedicated proximity electronic. MIRS OBOX is mounted on a dedicated bracket outside MMX eXploration module, with a nadir pointing (Fig. 6)

- An Electronic Box (EBOX) (Fig. 9A) containing the low-voltage power supply board (LVPS) (Fig. 9B) and the interface control unit board (ICU) (Fig. 9B). MIRS EBOX is located inside MMX exploration module (Fig. 6)
- An Interconnection harness linking the EBOX to the OBOX.

The OBOX is thermally uncoupled from the interface bracket. Two radiators ensure a passive cooling of the OBOX:

- 1 Dedicated to the spectrometer.
- 1 Dedicated to the detector package.

An open–close mechanism called dust cover is implemented on the MIRS OBOX entrance to protect the spectrometer from dust contamination (Fig. 8A).

The optical alignment is mechanically ensured with a stiff foot called Reference foot and a flexible one, i.e., a bipod called Axis foot. The third foot is mounted with regard to the Detector package center of mass. Figure 8B shows the external mechanical interfaces on the MIRS OBOX, while Fig. 8C shows the inside of the OBOX and the optical layout.

The EBOX (Fig. 9A) is the electronic box of the MIRS-F spectrometer. Its mass is about 1.2 kg. This unit is thermally coupled to the spacecraft descent module and is black anodized on its external surfaces. Figure 9 shows the two-subunits of the EBOX, i.e., the LVPS and the ICU.

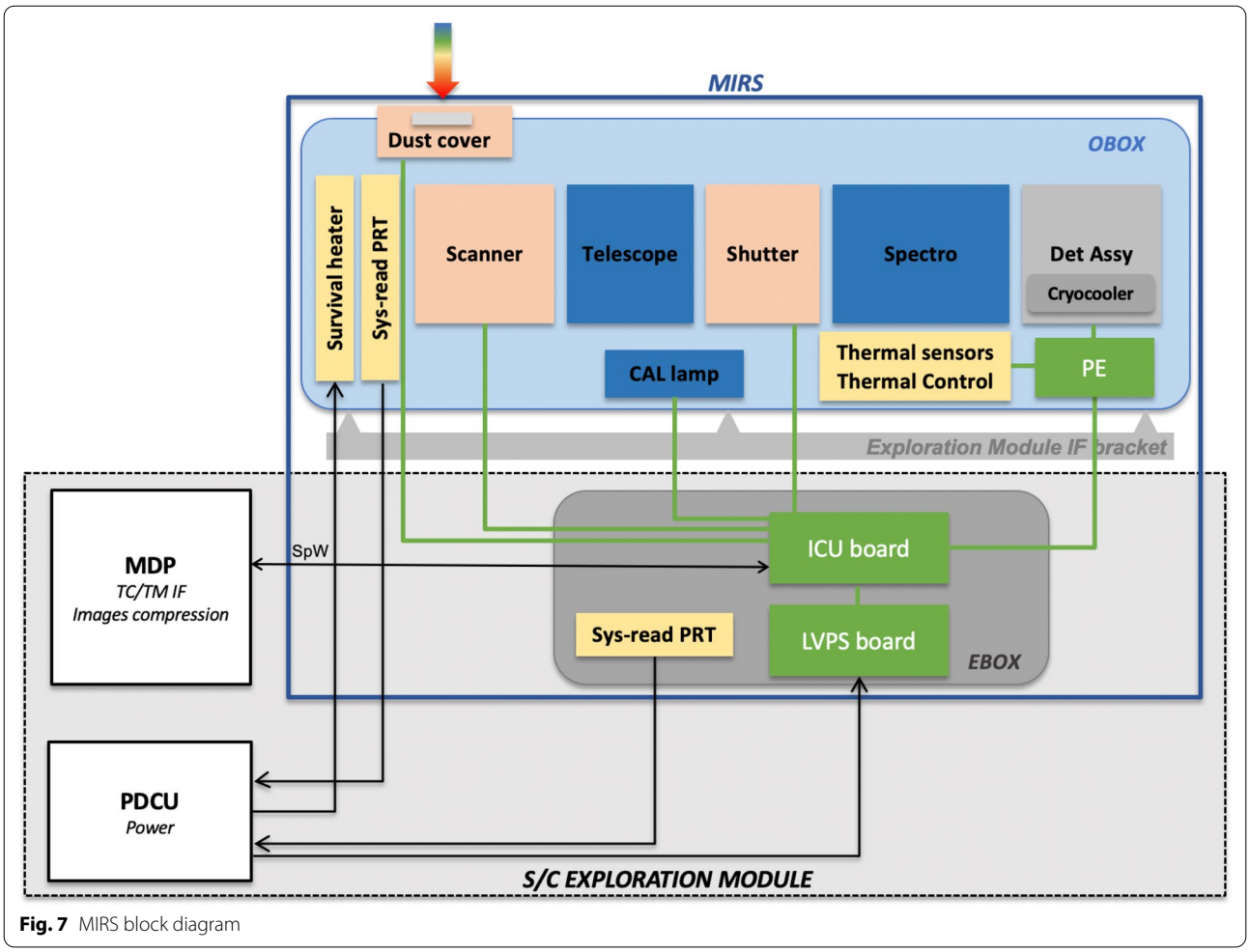

Fig. 7 MIRS block diagram

MIRS data shall be composed of:

- Science data are 2D raw data (Phobos, Deimos, Mars).
- Calibration data are 2D images of dark (shutter activated) and 2D images with the calibration source.
- Housekeepings (temperature, currents and voltage, statuses).

The instrument will produce 2D data cubes (λ, y) with typically images of 256×200 px^2.

MIRS has a data interface with the Mission Data Processor (MDP) which also has a data interface with the MMX spacecraft Management Unit (SMU) and the Mission Data Recorder (MDR). All telemetry data will be first transferred into the MDR via MDP without any compression. Telemetry data will be reloaded from MDR to MDP for the compression process (CCSDS122.0-B-1 standard).

MIRS mechanisms

Three mechanisms are implemented in MIRS.

Scanner mechanism

The along-track scanner mechanism (Fig. 10) is used to adjust ground speed with respect to the line of sight and also to reach specific phase angles. It is a single-axis scanner. A cam and lever mechanism transforms the rotation of the stepper geared motor to obtain the mirror movement. The full mechanical angular science stroke is $[-10°, +10°]$ (which allows a $[-20°, +20°]$ optical range for MIRS line of sight). The equipment is also able to target a calibration position at $+17°$. Mirror hinge is made with 2 cantilevered flexural pivots. No angular sensor in the equipment. The main characteristics are:

- Dimensions: $50 \times 40 \times 80$ (mm).
- Mass: 190 g.
- Power: Operating 1.5 W.
- Temperature range: [-50, + 60] °C.
- Position knowledge: ± 0.35 mRad.
- Position resolution: ± 40 µRad in full step mode.

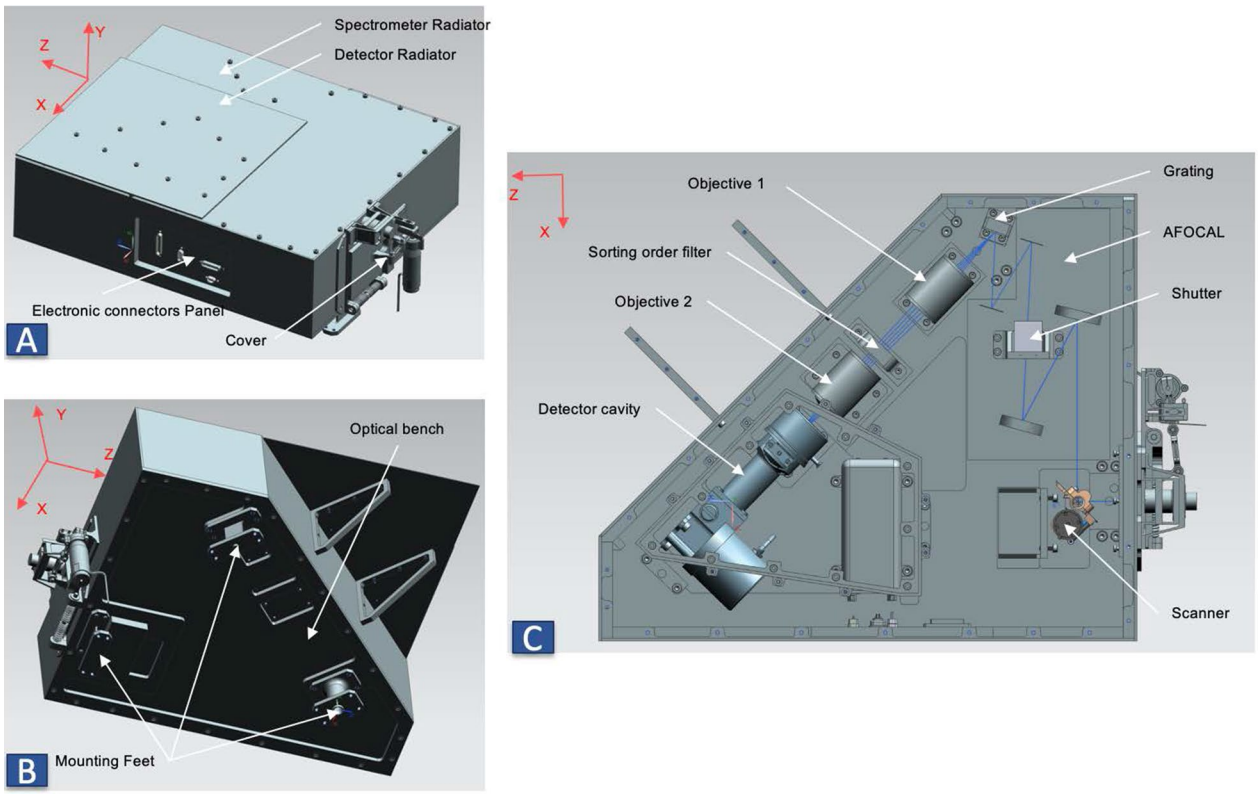

Fig. 8 MIRS OBOX external interface (**A** and **B**) and MIRS optical layout (**C**)

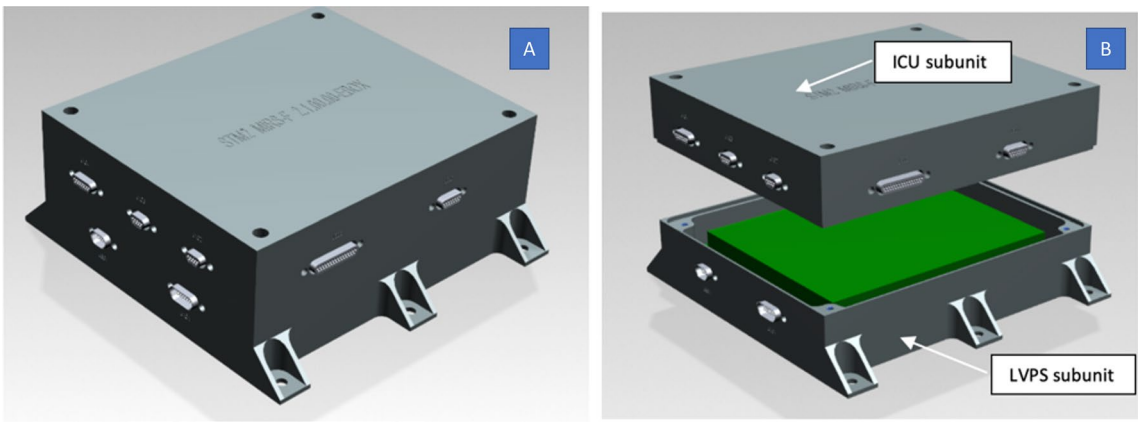

Fig. 9 MIRS EBOX. Assembled view (**A**), separated view (**B**)

Shutter mechanism

The MIRS shutter mechanism (Fig. 11) masks the spectrometer entrance slit (1×10 mm^2) in order to allow background acquisitions that can be subtracted to the science data. The design has a high space heritage and has already been qualified and flown on different space instruments: DIRS/Cassini-Huygens, OMEGA/Mars Express, VIRTIS/Venus Express and Rosetta, SuperCam/NASA Mars 2020 mission. The mechanism concept is based on a mono-stable actuator using steppers and permanent magnets: it keeps one stable position when the actuator is un-energized. The main characteristics are:

- Dimensions: $20 \times 20 \times 24$ (mm).

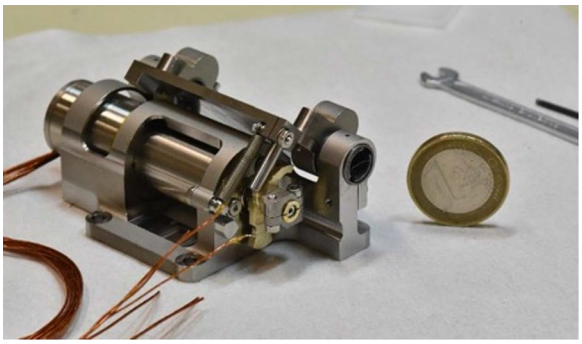

Fig. 10 MIRS scanner mechanism

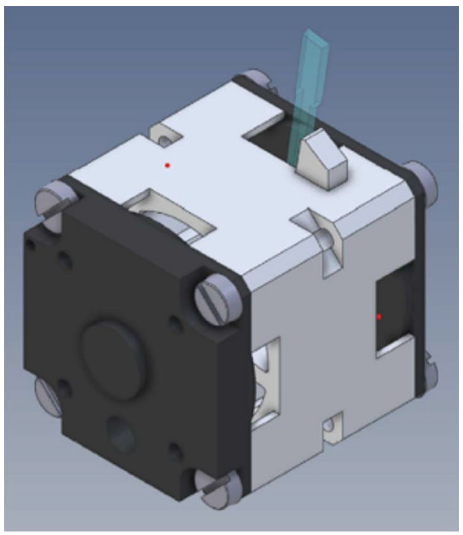

Fig. 11 MIRS shutter mechanism layout

- Mass: < 50 g.
- Low power consumption: < 1 W.
- Blade angular stroke: 20° − 0/ + 5°.
- Number of actuations > 1 million
- Temperature range: − 50 °C to 60 °C (has been used down to 150 K).

Cover mechanism

The MIRS cover mechanism (Fig. 12) closes the optical entrance (~ 50 × 90 mm^2) to protect optics from dust during landing phases on Phobos surface. The design is based on a space qualified Phytron moto-reduction system and a 3 bars mechanism. It allows opening and closing the cover (5 actuations). The cruise stable position is obtained with actuator in un-energized mode when the connecting rods are aligned. The cover mechanism is also

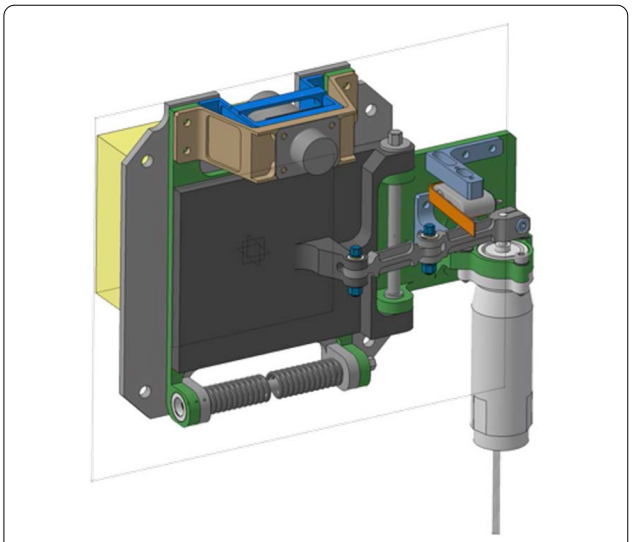

Fig. 12 MIRS cover concept

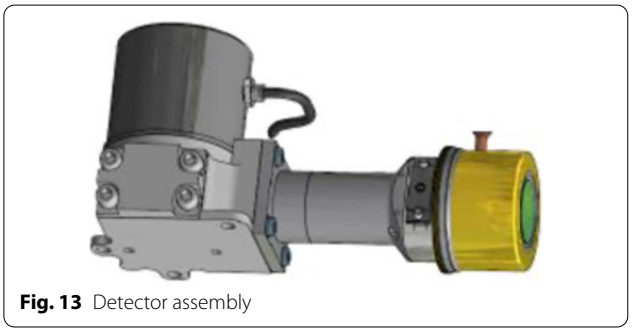

Fig. 13 Detector assembly

equipped with an additional HDRM (hold down release mechanism) to prevent failure mode due to dust intrusion inside cover or moto-reduction system. The main characteristics are:

- Dimensions: 200 × 130 × 45 (mm).
- Mass: < 500 g.
- Power: operating 8 W/30 s, emergency 10 W/10 min.
- Cover angular stroke: 0°–120°.
- Number of actuations: 5.
- Temperature range: − 50 °C to + 120 °C.

MIRS detector

The MIRS detector (Fig. 13) is based on COTS SWIR hybrid CMOS detector (Neptune) developed by Lynred and delivered with a cryocooler by Ricor (K508 reference). This assembly has already been used for several space missions and is fully qualified. The estimated lifetime of this cryocooler (of about 10,000 h) is well adapted to the MIRS operation lifetime requirements (estimated

operations duration of about 2000 h). The volume is around $138 \times 56 \times 70$ mm.

The detector format is 500 columns by 256 lines with square pixels of 30 μm pitch, sensitive to 0.45–3.8 μm made of photovoltaic diode in HgCdTe coupling via indium bump to a ROIC allowing different types of readout, gain and integration time control.

Its nominal working temperature is 110 K, with active cooling. To reduce background a cold pupil around 120 K is physically present in the cryostat. Thanks to backside illumination and anti-reflection coating optimized in the optical bandwidth, the quantum efficiency is up to 0.8, insuring high sensitivity, and low PRNU (< 20%). The dark current @110 K is given under 62.5 ke/s (n-on-p technology).

The ROIC allows the readout of one image frame while the next is under integration, two independent readout output may be programmed to decrease the readout time. The gain of each line may be programmable with low and high gain to optimized the readout noise with the signal, typically the noise is < 150 e with integrated charge of 0.5 Me and < 340 e with 2.5 Me, respectively. The maximum readout frequency of each single output is 8 MHz, allowing a minimal readout time of 3.2 ms for the whole area. The windowing readout mode is possible by programming the serial register of the ROIC, 1 indicates a line to be read (then the whole pixel of the line as to be red) and 0 indicates a line to be swapped out (during the programming of the ROIC, the gain of each line is chosen).

For the purpose of MIRS, only one half of the total sensitive surface will be used, leading to a readout of 250×256 pixels. The register is programmed at each power-on of the ROIC, the integration time is then managed by a single input signal. Proximity electronics inherited from previous instrument will only use one output @1 MHz with 12 bits ADC.

The detector has 2 integrated temperature sensors, one of them is used for the control of the cryocooler, and both will be monitored. A specific proximity electronics close to the cryostat is connected to the detector via a flex-ribbon to minimize the thermal link. It will insure the management of the bias polarization of the detector, the digitalization of the video signal and temperature sensor and the management of the cryocooler. A specific thermal strap links the cryocooler to a dedicated radiator to dissipate the 4–8 W needed to cool down the detector head.

Thermal architecture

OBOX is an external onboard subunit and thus sees spacecraft external thermal environment (Fig. 14). OBOX is located on an MMX bracket on which it is thermally insulated in a semi enclosure (on the + Y side of the spacecraft (S/C)). OBOX lateral sides are radiatively insulated, thanks to MLIs. OBOX is split in two thermal zones: a "warm" zone containing the cryocooler and a "cold" zone containing the spectrometer and the optical components.

The cryocooler is a Ricor K508 Stirling rotary cryogenic cooling machine which maintains the FPA at 110 K during science operations. OBOX + Y side has a "warm" radiator which evacuates the cryocooler heat dissipation. The cryocooler and "warm" radiator assembly are thermally insulated from the spectrometer.

A "cold" radiator is providing to the spectrometer an operating temperature below 250 K. OBOX mechanisms are thermally insulated from the optical bench and directly linked to this radiator. A survival system composed by heaters and mechanical thermal switches prevents OBOX from being colder than 230 K when MIRS is not operating.

EBOX is an internal onboard subunit. It is located inside MMX cavity and is thermally coupled to a S/C internal panel thanks to several screws and to thermal filler. EBOX is black painted in order to be radiatively coupled with S/C internal cavity walls.

Both MIRS subunits have one thermometer read by MMX system at any time, and several internal sensors read by MIRS when operating.

Electrical architecture

MIRS is composed of three electronics boards: one located inside the optical box (OBOX), and the two others inside the electronics box (EBOX). These electronics boards (Fig. 15) are:

- The low-voltage power supply board (LVPS) which generates, from an unregulated 32–50 V primary bus (provided by the power distribution control unit), all secondary voltages needed to supply the different subsystems of MIRS instrument. This board is located inside the EBOX.
- The interface control unit board (ICU) which accommodates a reprogrammable FPGA to manage raw data handling and storage, and TM/TC communication with the mission data processor (MDP) through a redundant SpaceWire link (SpW). The ICU board controls all mechanisms (scanner, dust cover, shutter), switch on/off the calibration lamp, controls the Neptune detector and its readout electronics. The ICU includes also two full bridges motor drivers to control step motors dedicated to dust cover and scanner, and a slow ADC for housekeeping monitoring (component temperatures, sec-

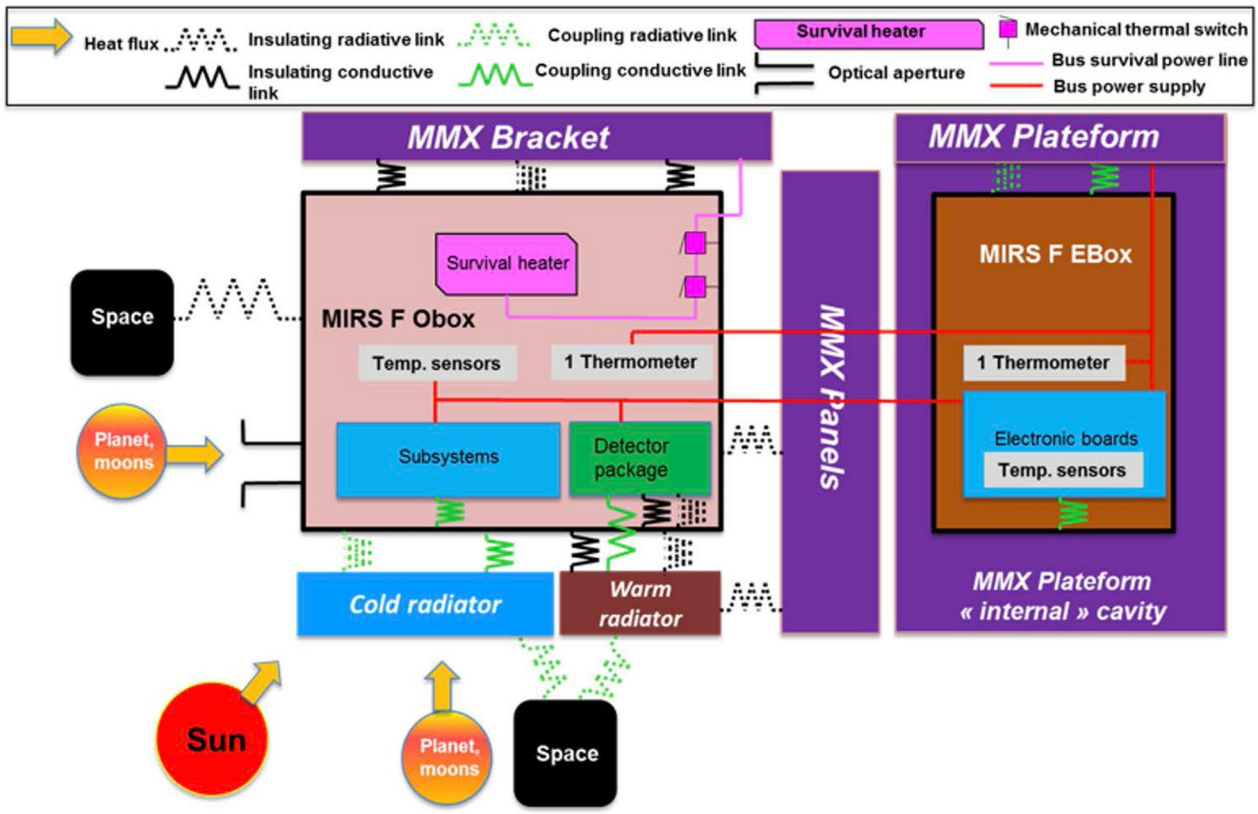

Fig. 14 MIRS thermal architecture

ondary voltages and primary current). This board is also located inside the EBOX.

- The readout electronics board of the MWIR detector. This board, called proximity electronics (PE), which accommodates a low-power 12-bit ADC at 1 MSps to sample one video output of the detector. A video amplifier is implemented on this board to match the dynamics of the detector signal to the ADC full-scale. The ADC integrates an 8-channel multiplexer, and the other channels are used to monitor the temperature of each mechanism and the spectrometer through a PT100 temperature sensor. A particular attention is given to PE board in order to provide very stable voltages for detector polarization by the use of linear regulator and common mode and differential filters. This board is located inside the OBOX, as close as possible to the detector.

Three shielded wire harnesses are used to connect the EBOX to the OBOX. The first one is used to provide all power signals to each mechanism, the two others connect directly the ICU board to the PE board for data and power signals. Low-voltage differential signaling (LVDS) transceivers are implemented on ICU and PE boards for digital data link transmission.

An 8-layer flex PCB is used to connect the PE board to both detector connectors: the first one (A) for analogue signals and the other one (B) for digital signals.

Digital electronics

The MIRS digital electronics is based on a FPGA device (Fig. 16), a NG-Medium from NaNoXPlore, and an embedded processor (soft IP, 8051 family). The main functions to be handle are communication with the MDP through Space Wire RMAP protocol, command dictionary support with TC/TLM (science data, housekeeping telemetry, and status telemetry), control of MIRS subsystems (detector and cryocooler, shutter, calibration lamp, scan mirror, dust cover), algorithm for image auto-exposure, data acquisition (2D images and housekeeping), and data processing.

The specificity of the design is its ability to perform the digital signal processing on 2D images (including image stacking, dark subtraction, region of interest extraction, spatial binning, spectral binning), on the fly, during detector read out and image transfer on Space Wire link. Additionally, detector readout and image transfer

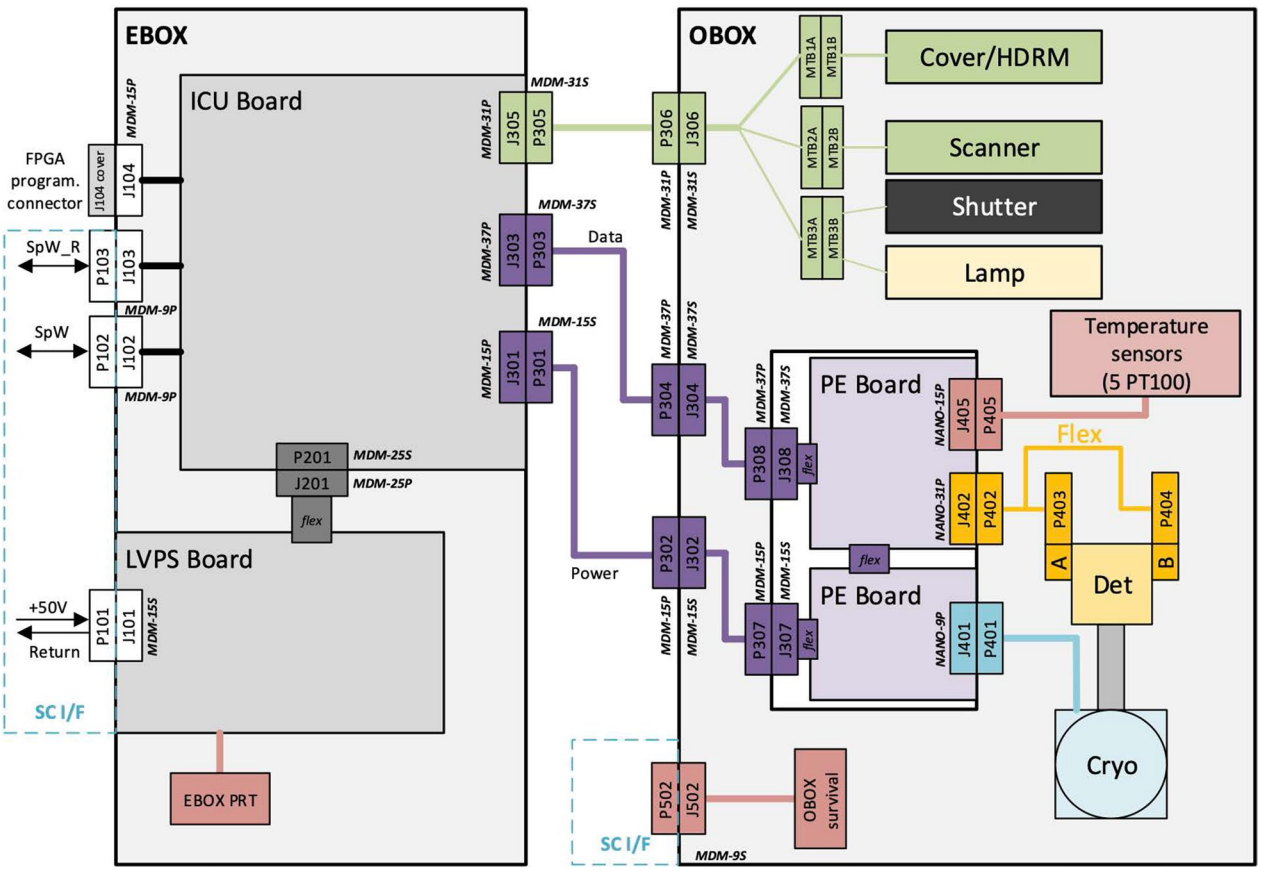

Fig. 15 MIRS electrical architecture

are performed during detector integration, in order to avoid (or minimize, depending on the integration time selected) dead time in the observation. The embedded processor is responsible for determining the best detector integration time and stacking factor to optimize SNR and avoid blurred images (Fig. 17). Also the processor has the capability to compute and update the scanner parameters (e.g., speed) during observations.

MIRS performances

MIRS performances have been simulated considering:

- Spectral resolution and spectral sampling.
- Spatial resolution.
- Signal-to-noise ratio.

In order to meet the spectral resolution requirement, the slit width is chosen so that its image on the focal plane convolved by the instrument PSF is spread on two pixels. The current optical design performances yield to a spectral sampled resolution less than 22 nm.

The spatial resolution is linked to the optical quality specified in terms of MTF (modulation transfer function) amplitude at Nyquist frequency. The requirement is > 8% over the field of view and spectral range. The instrument MTF is assessed by product of the optical FTM, the detector FTM and the smearing FTM.

Values @ Nyquist frequency:

- FTM optics: 0.4 (for both directions).
- FTM detector: 0.56 (for both directions).
- FTM smearing: takes into account S/C jitter (0.01° in 2 s) and Vsat.
- Across-track (S/C jitter only): 0.5 pixel ≥ instrument FTM = 0.2
- Along-track worst case: 0.5 pixel (S/C jitter) + 1 pixel (Vsat) ≥ instrument FTM = 0.13.

Therefore, the requirement is met for all cases.
The SNR is assessed considering:

- Spectrometer temperature: 250 K.
- Detector temperature: 110 K.

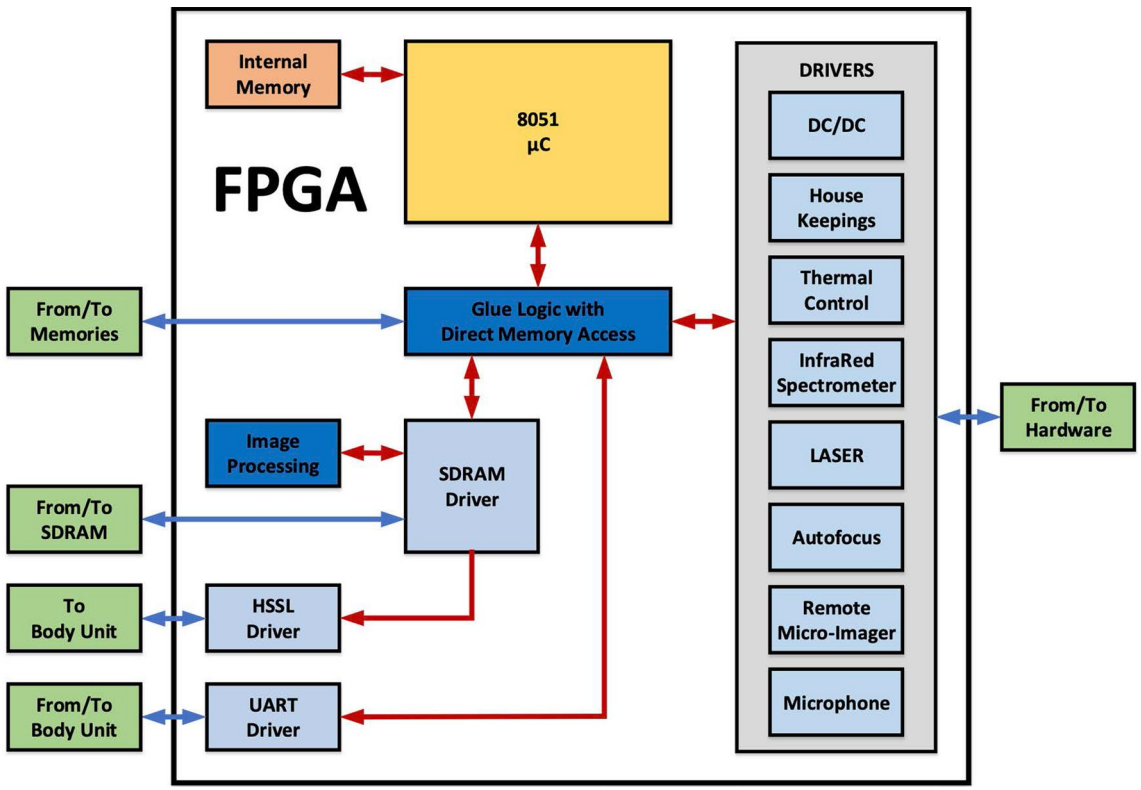

Fig. 16 FPGA general architecture

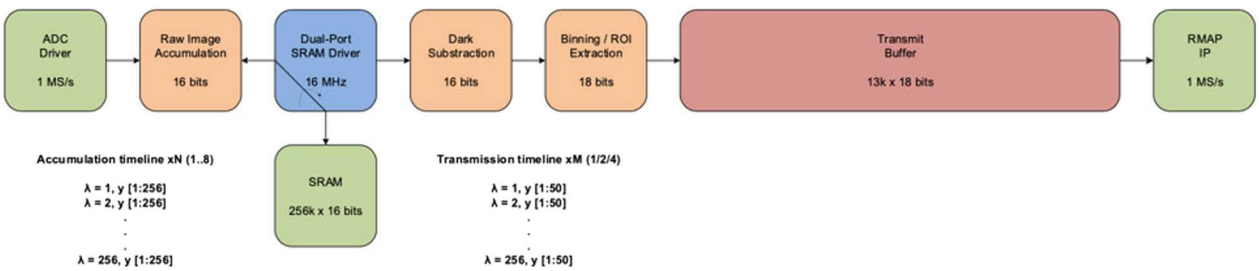

Fig. 17 Digital electronics detailed architecture

- Cold stop at 120 K.
- Reflected solar flux at 1.5 AU.
- Target albedo
- Lambertian surface.
- 30° sun illumination angle.
- Optical transmission.
- Detector performance (quantum efficiency, dark current, readout noise, quantification noise).

The SNR is limited by the maximum integration time allowable for an observation.

To calculate the maximum integration time, we need to consider two limits:

- Detector saturation that limits the elementary acquisition integration time,
- Pixel scroll due to MIRS movement with respect to the target in order to preserve the spatial resolution that limits the number of accumulations of elementary acquisitions.

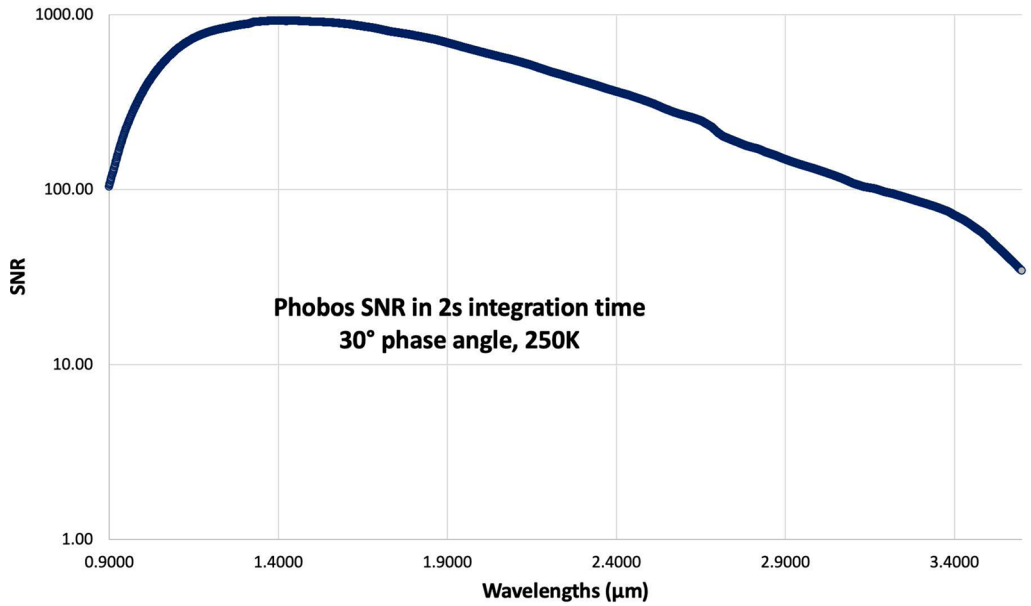

Fig. 18 Typical SNR profile for Phobos—QSO-M in 2-s integration time

For Phobos observations, the typical SNR profile is reported in Fig. 18. Note that SNR can be efficiently improved by integrating photons during a longer duration. For example, on QSO-M, the pixel scroll is higher than 3 s on 85% of the orbit.

For Mars observations, the different SNR profiles for a single accumulation are shown in Fig. 19. Depending on the various cases, the integration time is between 75 and 130 ms. The geometric nadir resolution is 2 km on ground (requirement is 10 km) so a spatial binning is possible to increase the SNR and save data volume.

MIRS observations

For several reasons, among which the fact that Phobos sphere of influence is very close to its surface, pure Keplerian motion of a satellite around it is not possible. Quasi-satellite orbits (QSOs) are therefore used and correspond to an MMX orbit around Mars with carefully set differences with Phobos orbit in order to induce a relative movement of MMX spacecraft around Phobos. Altitude varies during each revolution of MMX around Phobos and QSOs with various altitude ranges are defined in order to allow both global mapping and detailed analysis of landing site candidates (see paper by Nakamura et al. 2021).

Phobos

Phobos spectral observation by MIRS will consist of:

- A global mapping, performed from High and Medium altitude (see Nakamura et al. 2021 for orbit definition), to determine Phobos composition.
- A detailed observation of the landing site candidates, from medium and low altitude, to identify their thermal and compositional characteristics and provide the necessary information to select the 2 most interesting sites.
- A close observation of the 2 landing sites, during the vertical descent phase, to have a detailed spectral map to contribute to the selection of the sampling spot.

Global mapping

The first 2 months of Phobos observation will be performed from high- and medium-altitude equatorial quasi-satellite orbits (QSO), at a time when Sun elevation on Phobos (β angle) is low, which is favorable for the observation of North and South hemispheres. Priority is given to the zone within ± 30° latitudes, but higher latitudes (poles observation) are also important to settle the question of Phobos origin.

On the maps in Fig. 20, it is shown that high-resolution coverage of Phobos can be achieved by MIRS from medium equatorial quasi-satellite orbit. Coverage can be global from a 3D quasi-satellite orbit that allows visibility of high latitudes.

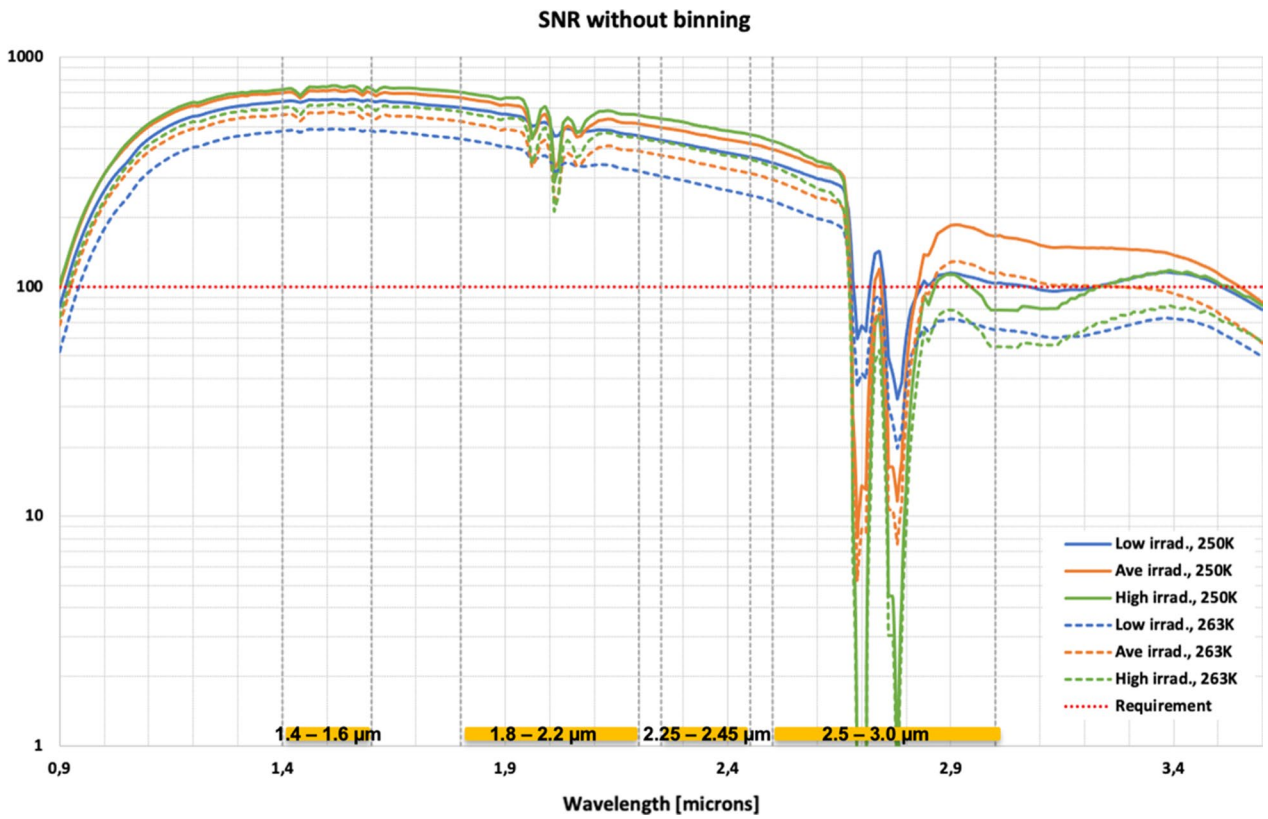

Fig. 19 Mars SNR in different radiance cases. SP#1: simulated MIRS SNR for the average Mars radiance observed by VIRTIS during Rosetta flyby (Coradini et al. 2010). SP#2: SNR for simulated Mars radiance at Ls 150° over dark highlands. SP#3: SNR for simulated Mars radiance at Ls 270° over Hellas Basin. SP#4: SNR for simulated Mars radiance at Ls 60° over the north plains

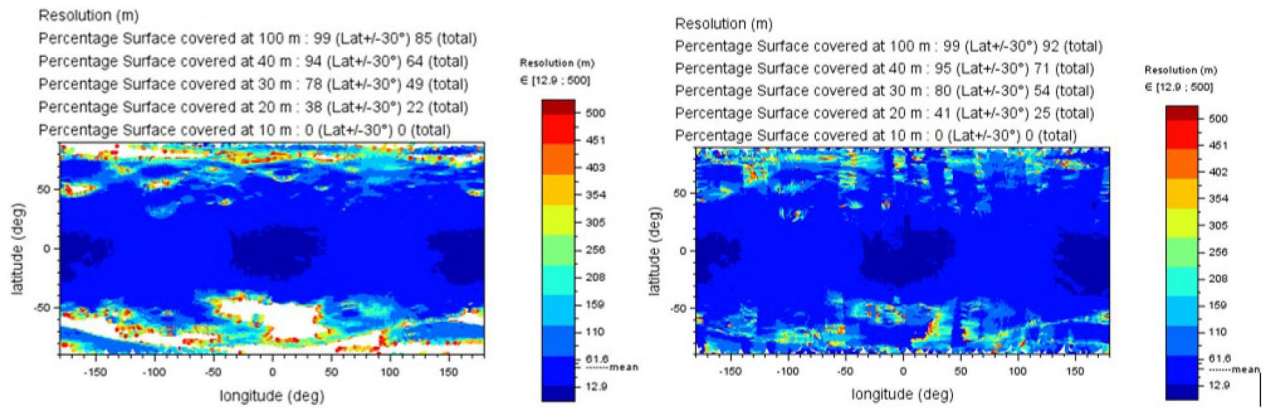

Fig. 20 Left: example of geometric resolution for equatorial QSO-M Nov 2025 (β = 3°). Most of Phobos is covered with high resolution. Zones in white cannot be observed because of MMX equatorial trajectory and Phobos flat shape on highest latitudes (poles). Right: example of geometric resolution for 3D-QSO-M Sep–Oct 2026 (β = − 6°). Highest latitudes (poles) can be observed thanks to MMX 3D trajectory that allows visibility of high latitudes

Landing sites candidates observation

Landing site candidates will be observed from medium (QSO-M) and low altitude equatorial quasi-satellite orbits (QSO-LA, -LB', -LC', Table 3). They will be in a flat zone for safe MMX landing and within latitudes ± 30°. Analysis of data collected from a given QSO will allow

Table 3 Different orbits for landing sites selection

QSO	Period	β (deg)	Distance to Phobos center (km)	Number of landing site candidates to observe
M	Mid-Nov/ mid-Dec 2025	3	50 × 100	50
LA	Mar 2026	− 21	30 × 50	20
LB′	Apr 2026	− 25	22 × 32	10
LC′	Jul 2026	− 17	20 × 27	5

to select the remaining best candidates to observe on the next QSO. It is therefore very important to ensure that data volume and data downlink rate are compatible with the timely analysis and selection process.

The lower the altitude is, the faster MMX relative speed to Phobos is. Therefore, for low-altitude QSOs MIRS along-track scanner will be used during observations to reduce the ground speed of MIRS Line of Sight projection on Phobos so that it is compatible with geometric pixel resolution and integration time.

In order to get as much information as possible for spectrographic and thermal inertia characterization, each site will be observed with several couples of phase angle and solar local time, in addition to the couple 10°/12 h.

Landing sites close observation during descent

During the 2 descent phases, MIRS will perform two 50-m large spectrographic maps, from altitudes 2 km down to 1 km, with a geometric resolution between 0.7 and 0.35 m. Additionally, to contribute to the selection of the sampling spot that will be chosen within a 2-m square zone centered on landing site, MIRS will perform a finer map from lowest possible altitude to get the best resolution.

Mars

In order to better understand the transport processes of dust and water between atmosphere and surface, large zones of Mars atmosphere will be observed several times with a time-resolution below 1 h. During most of its 3-year mission, MMX trajectory will be in quasi-satellite orbit around Phobos, which is very similar to Phobos orbit around Mars: nearly equatorial and circular, with a period of 7 h40'. Consequently, Mars observation slots will occur every 7 h40' at best and will last a maximum of 3 h50' (corresponding to the time MMX is above Sun-lighted part of Mars).

Each observation of a zone will consist of a series of west–east stripes: MIRS along-track scanner will move the line of sight along west–east while MMX spacecraft maneuver will perform the cross-track offsets before the acquisition of each stripe. To optimize coverage, it is proposed that MMX compensates during observations the yaw offset of the stripes induced by the small inclination of MMX orbit.

In Fig. 21, we present 3 examples of observations: on the left, a zone on the south hemisphere is observed 3 times with a time resolution of 45 min. On the center, a central zone is observed 5 times with a time resolution of 30 min: the longer the total time span is, the shorter the coverable west–east span of the zone is. On the right, a single observation of most of Mars disk lighted zone is performed. To gather further information on Mars atmosphere composition, MIRS will also perform various kinds of limb observations.

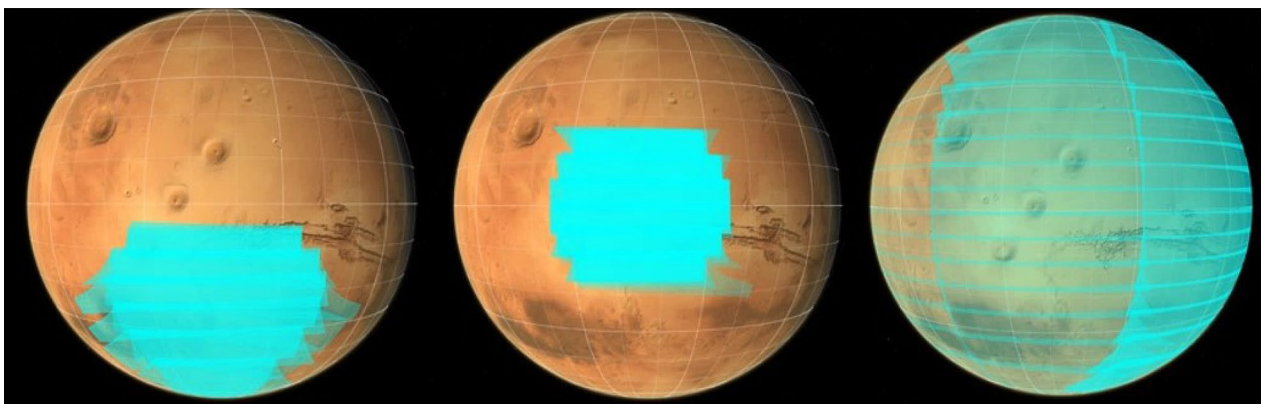

Fig. 21 Example of Mars observations on QSO-M Dec 2027. Left: 3 observations of South hemisphere with 45 min time resolution: 1h30 time span. Center: 5 observations of a central zone with 30-min time resolution: 2 h time span. Right: global coverage of lighted part of Mars

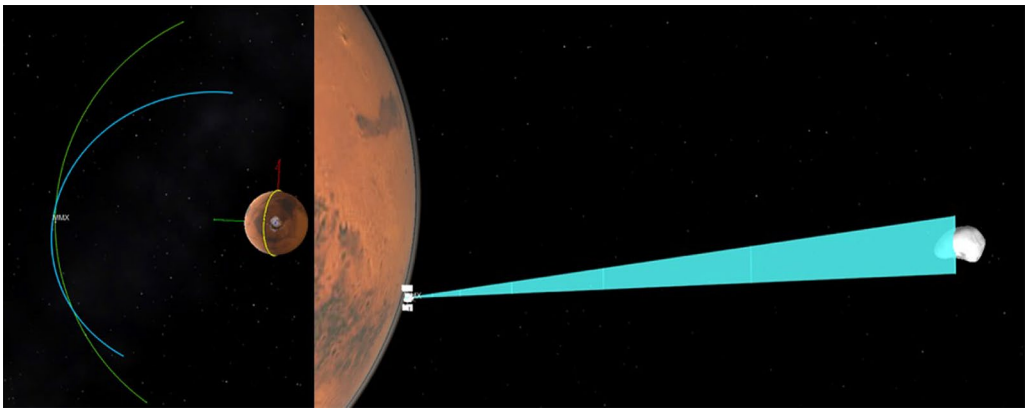

Fig. 22 Deimos observation by MIRS from an elliptical orbit. On the left, Deimos orbit in green and MMX orbit in blue. On the right, example of MIRS line of sight in blue pointing to Deimos at closest distance of 300 km (nadir resolution is 105 m)

Deimos

Deimos being around 2.5 times farther from Mars center than Phobos, it will be observed during multiple fly-bys, from the elliptical orbits of MMX around Mars (Fig. 22). Current baseline is that MMX will remain on each of the three foreseen orbits the necessary time to perform ten Deimos fly-bys.

It is a real challenge for observations as MMX relative velocity to Deimos being very high, distance will evolve very quickly, reducing the duration of observation slots with a geometric resolution below 100 m. A key issue is the setting of the minimum distance to Deimos: the farther the safer for MMX trajectory, the shorter the better for geometric resolution.

Conclusions

MIRS is an imaging spectrometer that uses the push-broom acquisition principle. The near-infrared wavelength range in 0.9–3.6 μm has been chosen to optimize the study the Phobos and Deimos surface composition as well Mars atmosphere with a spatial resolution of 20 m or better on Phobos surface. It will be also a fundamental instrument to evaluate sampling site candidates.

For Phobos, MIRS will allow to obtain a global mapping, performed from high and medium altitude. It will allow to investigate the surface composition as well the thermal characteristics and to provide, with observations during the closer orbits, the necessary information to select the most interesting sampling sites. MIRS will allow also to have a detailed spectral map to characterize the sampling spot with the close observation of the two landing sites, during the vertical descent phase down to a distance from the surface of at least 400 m. MIRS will allow to characterize the Deimos surface composition to investigate the compositional analogy with Phobos. MIRS will provide the first opportunity for investigating the Martian diurnal variation and the transport processes of dust and water vapor with time-resolved pictures of the atmospheric phenomena from the equatorial orbit.

The MIRS instrument together with the MMX payload and sample analysis will be able to clarify the origin of the Martian moons and may also be able to elucidate the process of the evolution of the Mars environment.

Abbreviations

ADC: Analog-to-digital convert; CMOS: Complementary metal oxide semiconductor; COTS SWIR: Commercial off-the-shelf short-wave InfraRed; CRISM: Compact reconnaissance imaging spectrometer for Mars; EBOX: Electronic BOX; FTM: Fonction de Transfert de Modulation; HiRISE: High-resolution imaging science experiment; HDRM: Hold down release mechanism; ICU: Interface control unit board; IMP: Imaging for Mars Pathfinder; IRTF: InfraRed telescope facility; ISM: Imaging spectrometer for Mars; LVPS: Low-voltage power supply; LVDS: Low-voltage differential signaling; MAWD: Mars atmospheric water detector; MDP: Mission data processor; MDR: Mission data recorder; MEX: Mars EXpress; MIRS: MMX-InfraRed spectrometer; MMX: Martian Moon eXploration; MR: Mission requirements; MRO: Mars reconnaissance orbiter; MTF: Modulation Transfert Fonction; OBOX: Optical BOX; OMEGA: Observatoire pour la Minéralogie, l'Eau, la Glace et l'Activité; OROCHI: Optical RadiOmeter composed of chromatic imagers; OVIRS: OSIRIS-REx visible and IR spectrometer; PE: Proximity electronics; PFS: Planetary Fourier spectrometer; QSO: Quasi-satellite orbit; QSO-M: Quasi-satellite orbit-medium; RMAP: Remote memory access protocol; ROIC: ReadOut integrated circuit; SMU: Spacecraft management unit; SNR: Signal-to-noise ratio; SPICAM: Spectroscopy for investigation of characteristics of the atmosphere of Mars; SPW: SPaceWire; SWIR: Short-wave InfraRed; VIRTIS: Visible InfraRed thermal imaging spectrometer.

Acknowledgements

We thank CNES for the financial support and collaboration to build MIRS instrument onboard MMX mission. MMX is developed by JAXA, with contributions from CNES, DLR and NASA. We thank the MMX JAXA teams for their efforts in defining and building the mission.

Authors' contributions

MAB, AD, SF, HN, TN, SA, PB, SC, MD, TG, LJ, JL, CL, FM contributed to the science input of the manuscript. JMR, PB, MLD, TI, YA, FC, BD, SG, RH-K, GH, CI, DK,

LL, AL, BLR, NNT, JP, LP, BQ, DZ contributed to the design and development of the instrument. ES contributed to the MIRS observations. All others provided feedback. All authors read and approved the final manuscript.

Funding
MIRS instrument is financed by CNES.

Availability of data and materials
None.

Declarations

Competing interests
The authors declare that they have no competing interest.

Author details
[1]LESIA-Observatoire de Paris, Université PSL, CNRS, Sorbonne Université, Université de Paris, 5 place Jules Janssen, 92195 Meudon, France. [2]CNES, Toulouse, France. [3]ISAS JAXA, Sagamihara, Japan. [4]Department of Geophysics, Tohoku University, Sendai Miyagi 980-8578, Japan. [5]CNES, Paris, France. [6]Ashikaga University, Ashikaga, Japan. [7]Université Grenoble Alpes, CNRS, IPAG, Grenoble, France. [8]Université de Paris, Institut de Physique du Globe de Paris, CNRS, Paris, France. [9]LATMOS/IPSL, UVSQ Université Paris-Saclay, Sorbonne Université, CNRS, Guyancourt, France. [10]CNRS, Observatoire Côte d'Azur, Nice, France. [11]Observatoire Midi-Pyrenées, Toulouse, France. [12]LAB Université de Bordeaux, Bordeaux, France. [13]Earth-Life Science Institute, Tokyo Institute of Technology, Tokyo, Japan. [14]University of Tokyo, Tokyo, Japan. [15]Laboratoire d'Astrophysique de Marseille, Marseille, France. [16]Rikkyo University, Tokyo, Japan. [17]NIAIST, Tokyo, Japan. [18]IRAP, Toulouse, France. [19]LPG, UMR CNRS 6112, Université de Nantes, Université d'Angers, Nantes, France. [20]Kyoto Sangyo University, Kyoto, Japan. [21]Japan Atomic Energy Agency, Tokai, Japan. [22]Hokkaido Information University, Ebetsu, Japan. [23]Aix Marseille Univ. CNRS, CNES, LAM, Marseille, France.

Received: 5 December 2020 Accepted: 23 April 2021
Published online: 06 December 2021

References

Aoki S, Sato Y, Giuranna M, Wolkenberg P, Sato TM, Nakagawa H, Kasaba Y (2018) Mesospheric CO_2 ice clouds on Mars observed by Planetary Fourier Spectrometer onboard Mars Express. Icarus 302:175–190. https://doi.org/10.1016/j.icarus.2017.10.047

Audouard J, Poulet F, Vincendon M, Milliken RE, Jouglet D, Bibring J-P, Gondet B, Langevin Y (2014) Water in the Martian regolith from OMEGA/Mars Express. J Geophys Res 119:1969–1989. https://doi.org/10.1002/2014JE004649

Bandfield JL, Piqueux S, Glotch TD, Shirley KA, Duxbury TC, Hill JR, Edwards, CS, Plaut JJ, Hamilton VE, Christensen PR (2018) Mars Odyssey THEMIS Observations of Phobos: New Spectral and Thermophysical Measurements. In: 49th Lunar and Planetary Science Conference 19–23 March 49, 2643

Basilevsky AT, Lorenz CA, Shingareva TV, Head JW, Ramsley KR, Zubarev AE (2014) The surface geology and geomorphology of Phobos. Planet Space Sci 102:95–118. https://doi.org/10.1016/j.pss.2014.04.013

Bell JF III, Maki JN, Mehall GL, Ravine MA, Caplinger MA, Bailey ZJ, Brylow S, Schaffner JA, Kinch KM, Madsen MB, Winhold A, Hayes AG, Corlies P, Tate C, Barrington M, Cisneros E, Jensen E, Paris K, Crawford K, Rojas C, Mehall L, Joseph J, Proton JB, Cluff N, Deen RG, Betts B, Cloutis E, Coates AJ, Colaprete A, Edgett KS, Ehlmann BL, Fagents S, Grotzinger JP, Hardgrove C, Herkenhoff KE, Horgan B, Jaumann R, Johnson JR, Lemmon M, Paar G, Caballo-Perucha M, Gupta S, Traxler C, Preusker F, Rice MS, Robinson MS, Schmitz N, Sullivan R, Wolff MJ (2021) The Mars 2020 perseverance rover mast camera zoom (Mastcam-Z) multispectral. Stereosc Imag Investig Space Sci Rev 217:24. https://doi.org/10.1007/s11214-020-00755-x

Bertaux JL, Gondet B, Lefvre F, Bibring JP, Montmessin F (2012) First detection of O_2 1.27 μm nightglow emission at Mars with OMEGA/MEX and comparison with general circulation model predictions. J Geophys Res E Planets 117. https://doi.org/10.1029/2011JE003890

Bibring JP, Ksanfomaliti LV, Langevin I, Moroz VI, Combes M, Grigor'ev AV, Khatuntsev IV, Nikol'Skii IuV, Zharkov AV (1989) Composite KRFM-ISM spectrum of Phobos (0.315–3.1 μm). Adv Space Res 12:13–16. https://doi.org/10.1016/0273-1177(92)90313-M

Bibring J-P, Langevin Y, Soufflot A, Combes C, Cara C, Drossart P, Encrenaz Th, Erard S, Forni O, Gondet B, Ksanfomalfty L, Lellouch L, Masson Ph, Moroz V, Rocard F, Rosenqvist J, Sotin C (1992) Results from the ISM experiment. Nature 341:591–593. https://doi.org/10.1038/341591a0

Burns JA (1992) Contradictory clues as to the origin of the Martian moons. In: Kieffer HH, Jakosky BM, Snyder CW, Matthews MS (eds) Mars. University of Arizona Press, Tucson, Arizona, USA, pp 1283–1301

Canup R, Salmon J (2018) Origin of Phobos and Deimos by the impact of a Vesta-to- Ceres sized body with Mars. Sci Adv 4(4). https://doi.org/10.1126/sciadv.aar6887

Ceamanos X, Douté S, Fernando J, Schmidt F, Pinet P, Lyapustin A (2013) Surface reflectance of Mars observed by CRISM/MRO: 1. Multi-angle approach for retrieval of surface reflectance from CRISM observations (MARS-ReCO). J Geophys Res Planets 118(3):514–533. https://doi.org/10.1029/2012JE004195

Chaffin M, Deighan J, Schneider NM, Stewart AIF (2017) Elevated atmospheric escape of atomic hydrogen from Mars induced by high-altitude water. Nat Geosci 10:174. https://doi.org/10.1038/ngeo2887

Clancy RT, Sandor BJ (1998) CO_2 ice clouds in the upper atmosphere of Mars. Geophys Res Lett 25(4):489–492. https://doi.org/10.1029/98GL00114

Clancy RT, Sandor BJ, Wolff MJ, Smith MD, Lefèvre F, Madeleine J-B, Forget F, Murchie SL, Seelos FP, Seelos KD, Nair H, Toigo AD, Humm D, Kass DM, Kleinböhi A, Heavens N (2013) Correction to Extensive MRO CRISM observations of 1.27 μm O_2 airglow in Mars polar night and their comparison to MRO MCS temperature profiles and LMD GCM simulations. J. Geo. Res. 118:1148. https://doi.org/10.1002/jgre.20073

Clancy T, Smith MD, Lefèvre F, McConnochie TH, Sandor BJ, Wolff MJ, Lee SW, Murchie SL, Toigo AD, Nair H, Navarro T (2017) Vertical profiles of Mars 1.27 μm O_2 dayglow from MRO CRISM limb spectra: Seasonal/global behaviors, comparisons to LMDGCM simulations, and a global definition for Mars water vapor profiles. Icarus 293:132–156. https://doi.org/10.1016/j.icarus.2017.04.011

Clancy RT, Wolff MJ, Smith MD, Kleinböhl A, Cantor BA, Murchie SL, Toigo AD, Seelos K, Lefèvre F, Montmessin F, Daerden F, Sandor BJ (2019) The distribution, composition, and particle properties of Mars mesospheric aerosols: an analysis of CRISM visible/near-IR limb spectra with context from near-coincident MCS and MARCI observations. Icarus 328:246–273. https://doi.org/10.1016/j.icarus.2019.03.025

Clark RN, Cruikshank DP, Jaumann R, Brown RH, Stephan K, Dalle Ore CM, Eric Livo K, Pearson N, Curchin JM, Hoefen TM, Buratti BJ, Filacchione G, Baines KH, Nicholson PD (2012) The surface composition of Iapetus: mapping results from Cassini VIMS. Icarus 218:831–860. https://doi.org/10.1016/j.icarus.2012.01.008

Combes M, Cara C, Drossart P, Encrenaz T, Lellouch E, Rosenqvist J, Bibring J-P, Erard S, Gondet B, Langevin Y, Soufflot A, Moroz VI, Grygoriev AV, Ksanfomality LuV, Nikolsky YV, Sanko NF, Titov DV, Forni O, Masson P, Sotin C (1991) Martian atmosphere studies from the ISM experiment. Planet Space Sci 39:189–197. https://doi.org/10.1016/0032-0633(91)90141-V

Craddock RA (2011) Are Phobos and Deimos the result of a giant impact? Icarus 211(2):1150–1161. https://doi.org/10.1016/j.icarus.2010.10.023

Daerden FL, Neary S, Vinscardy AG, Muñoz RT, Clancy MD, Smith T, Encrenaz AF (2019) Mars atmospheric chemistry simulations with the GEM-Mars general circulation model. Icarus 326:197–224. https://doi.org/10.1016/j.icarus.2019.02.030

Delbo M, Mueller M, Emery JP, Rozitis B, Capria MT (2015) Asteroid Thermophysical Modeling. In: Michel P et al (eds) Asteroids IV. University of Arizona Press, Tucson, pp 107–128

DellaGiustina DN et al (2019) Properties of rubble-pile asteroid (101955) Bennu from OSIRIS-REx imaging and thermal analysis. Nat Astron 3:341–351. https://doi.org/10.1038/s41550-019-0731-1

Donaldson H et al. (2016) Spectral characterization of desiccated phyllosilicate samples as analogues for Phobos and primitive solar system bodies. 2016. In: 47th Lunar and Planetary Science Conference 2184. https://doi.org/10.1016/j.icarus.2018.10.018

Encrenaz T, Fouchet T, Melchiorri R, Drossart P, Gondet B, Langevin Y, Bibring JP, Forget F, Bézard B (2006) Seasonal variations of the martian CO over Hellas as observed by OMEGA/Mars express. Astron Astrophys 459:265–270. https://doi.org/10.1051/0004-6361:20065586

Erard S, Mustard J, Murchie S, Bibring JP, Cerroni P, Coradini A (1994) Martian aerosols: near-infrared spectral properties and effects on the observation of the surface. Icarus 111(2):317–337. https://doi.org/10.1006/icar.1994.1148

Fedorova A, Korablev O, Perrier S, Bertaux JL, Lefevre F, Rodin A (2006) Observation of O_2 1.27 μm dayglow by SPICAM IR: seasonal distribution for the first Martian year of Mars Express. J Geophys Res Planets 111: E09S07. https://doi.org/10.1029/2006JE002694

Fernando J, Schmidt F, Ceamanos X, Pinet P, Douté S, Daydou Y (2013) Surface reflectance of Mars observed by CRISM/MRO: 2. Estimation of surface photometric properties in Gusev Crater and Meridiani Planum. J Geophys Res Planets 118(3):534–559. https://doi.org/10.1029/2012JE004194

Forget F, Spiga A, Dolla B, Vinatier S, Melchiorri R, Drossart P, Gendrin A, Bibring J-P, Langevin Y, Gondet B (2007) Remote sensing of surface pressure on Mars with the Mars Express/OMEGA spectrometer: 1. Retrieval method. J Geophys Res Planets 112:8. https://doi.org/10.1029/2006JE002871

Fraeman AA, Murchie SL, Arvidson RE, Clark RN, Morris RV, Rivkin AS, Vilas F (2014) Spectral absorptions on Phobos and Deimos in the visible/near infrared wavelengths and their compositional constraints. Icarus 229:196–205. https://doi.org/10.1016/j.icarus.2013.11.021

Gaskell RW (2011) Gaskell Phobos Shape Model V1.0. VO1-SA-VISA/VISB-5-PHOBOSSHAPE-V1.0. NASA Planetary Data System

Gatley I, Kieffer H, Miner E, Neugebauer G (1974) Infrared observations of PHOBOS from Mariner 9. Astrophys J 190:497–508. https://doi.org/10.1086/152902

Spiga A, Forget F, Dolla B, Vinatier S, Melchiorri R, Drossart P, Gendrin A, Bibring J-P, Langevin Y, Gondet B (2007) Remote sensing of surface pressure on Mars with the Mars Express/OMEGA spectrometer: 2 Meteorological maps. J Geophys Res Planets 112(E8). https://doi.org/10.1029/2006JE002870

Giuranna M, Roush TL, Duxbury T, Hogan RC, Carli C, Geminale A, Formisano V (2011) Compositional interpretation of PFS/MEX and TES/MGS thermal infrared spectra of Phobos. Planet Space Sci 59(13):1308–1325. https://doi.org/10.1016/j.pss.2011.01.019

Glotch T, Edwards C, Ebel D (2015) Spectral properties of Phobos from the Mars Global Surveyor Thermal Emission Spectrometer: evidence for water and carbonate. Lunar Planet. Sci. XLVI, Abstract #2587. Lunar and Planetary Institute, Houston

Grott M et al (2019) Low thermal conductivity boulder with high porosity identified on C-type asteroid (162173) Ryugu. Nat Astron 3:971–976. https://doi.org/10.1038/s41550-019-0832-x

Grundy WM, Fink U (1992) Deimos: a reddish, D-type asteroid spectrum. In Asteroids, Comets, Meteors 1991, pp. 215–218. Lunar and Planetary Institute

Gundlach B, Blum J (2013) A new method to determine the grain size of planetary regolith. Icarus 223:479–492. https://doi.org/10.1016/j.icarus.2012.11.039

Hansen BMS (2018) A dynamical context for the origin of Phobos and Deimos. Mon Not R Astron Soc 475(2):2452–2466. https://doi.org/10.1093/mnras/stx3361

Heavens NG, Kleinböhl A, Chaffin MS, Halekas JS, Kass DM, Hayne PO, McCleese DJ, Piqueux S, Shirley JH, Schofield JT (2018) Hydrogen escape from Mars enhanced by deep convection in dust storms. Nature Astronomy 2:126–132. https://doi.org/10.1038/s41550-017-0353-4

Hesselbrock AJ, Minton DA (2017) An ongoing satellite-ring cycle of Mars and the origins of Phobos and Deimos. Nat Geosci 10(4):266–269. https://doi.org/10.1038/ngeo2916

Hyodo R, Genda H, Charnoz S, Rosenblatt P (2017) On the impact origin of Phobos and Deimos. I. Thermodynamic and physical aspects. Astrophys J 845(2):125. https://doi.org/10.3847/1538-4357/aa81c4

Hyodo R, Genda H, Charnoz S, Pignatale FCF, Rosenblatt P (2018) On the impact origin of Phobos and Deimos. IV. Volatile Depletion. Astrophys J 860(2):150. https://doi.org/10.3847/1538-4357/aac024

Hyodo R, Kurosawa K, Genda H, Usui T, Fujita K (2019) Transport of impact ejecta from Mars to its moons as a means to reveal Martian history. Sci Rep 9:19833. https://doi.org/10.1038/s41598-019-56139-x

Ignatiev NI, Grassi D, Zasova LV (2005) Planetary Fourier spectrometer data analysis: fast radiative transfer models. Planet Space Sci 53:1035. https://doi.org/10.1016/j.pss.2004.12.009

Kaula WM (1964) Tidal dissipation by solid friction and the resulting orbital evolution. Rev Geophys Space Phys 2:661–685. https://doi.org/10.1029/RG002i004p00661

Kührt E, Giese B (1989) A thermal model of the Martian satellites. Icarus 81:102–112

Kührt E, Giese B, Keller HU, Ksanfomality LV (1992) Interpretation of the KRFM-infrared measurements of PHOBOS. Icarus 96:213–218. https://doi.org/10.1016/0019-1035(92)90075-I

Kuramoto K et al (2021) Martian moons exploration MMX: sample return mission to Phobos elucidating formation processes of habitable planets. Earth Planets Space. https://doi.org/10.1186/s40623-021-01545-7.

Laskar J, Robutel P (1993) The chaotic obliquity of the planets. Nature 361(6413):608–612. https://doi.org/10.1038/361608a0

Lauretta DS et al (2015) The OSIRIS-REx target asteroid (101955) Bennu: constraints on its physical, geological, and dynamical nature from astronomical observations. Meteorit Planet Sci 50:834–849. https://doi.org/10.1111/maps.12353

Lefèvre F, Lebonnois S, Montmessin F, Forget F (2004) Three-dimensional modeling of ozone on Mars. J Geophys Res E Planets 109. https://doi.org/10.1029/2004JE002268

Lucey PG, Keil K, Whitely R (1998) The influence of temperature on the spectra of the A-asteroids and implications for their silicate chemistry. JGR 103:5865–5871. https://doi.org/10.1029/97JE03691

Lunine JI, Neugebauer G, Jakosky BM (1982) Infrared observations of PHOBOS and Deimos from Viking. J Geophys Res 87:10297–10305. https://doi.org/10.1029/JB087iB12p10297

Määttänen A, Fouchet T, Forni O, Forget F, Savijärvi H, Gondet B, Melchiorri R, Langevin Y, Formisano V, Giuranna M, Bibring JP (2009) A study of the properties of a local dust storm with Mars Express OMEGA and PFS data. Icarus 201(2):504–516. https://doi.org/10.1016/j.icarus.2009.01.024

Maltagliati L, Titov DV, Encrenaz T, Melchiorri R, Forget F, Garcia-Comas M, Keller HU, Langevin Y, Bibring J-P (2008) Observations of atmospheric water vapor above the Tharsis volcanoes on Mars with the OMEGA/MEx imaging spectrometer. Icarus 194:53–64. https://doi.org/10.1016/j.icarus.2007.09.027

Maltagliati L, Titov DV, Encrenaz T, Melchiorri R, Forget F, Keller HU, Bibring J-P (2011) Annual survey of water vapor behavior from the OMEGA mapping spectrometer onboard Mars Express. Icarus 213:480–495. https://doi.org/10.1016/j.icarus.2011.03.030

Maltagliati L, Montmessin F, Korablev O, Fedorova A, Forget F, Määtänen A, Lefèvre F, Bertaux J-L (2013) Annual survey of water vapor vertical distribution and water-aerosol coupling in the martian atmosphere observed by SPICAM/MEx solar occultations. Icarus 223:942–962. https://doi.org/10.1016/j.icarus.2012.12.012

Maurice S, Wiens RC, Bernardi P, Caïs P, Robinson S et al (2021) The SuperCam Instrument suite on the Mars 2020 Rover: science objectives and Mast-Unit Description. Space Sci Rev 217:47. https://doi.org/10.1007/s11214-021-00807-w

Montmessin F, Forget F, Rannou P, Cabane M, Haberle RM (2004) Origin and role of water ice clouds in the martian water cycle as inferred from a general circulation model. J Geophys Res 109:E10004. https://doi.org/10.1029/2004JE002284

Montmessin F, Bertaux J-L, Quémerais E, Korablev O, Rannou P, Forget F, Perrier S, Fussen D, Lebonnois S, Rébérac A, Dimarellis E (2006) Subvisible CO_2 ice clouds detected in the mesosphere of Mars. Icarus 183:403–410. https://doi.org/10.1016/j.icarus.2006.03.015

Montmessin F, Korablev O, Lefèvre F, Bertaux JL, Fedorova A, Trokhimovskiy A, Chaufray JY, Lacombe G, Reberac A, Maltagliati L, Willame Y, Guslyakova S, Gérard JC, Stiepen A, Fussen D, Mateshvili N, Määttänen A, Forget F, Witasse O, Leblanc F, Vandaele AC, Marcq E, Sandel B, Gondet B, Schneider N, Chaffin M, Chapron N (2017) SPICAM on Mars Express: a 10 year in-depth survey of the Martian atmosphere. Icarus 297:195–216. https://doi.org/10.1016/j.icarus.2017.06.022

Moroz J, Shade U, Wasch R (2000) Reflectance spectra of Olivine-orthopyroxene-bearing assemblages at decreased temperatures: implications for remote sensing of asteroids. Icarus 147:79. https://doi.org/10.1006/icar.2000.6430

Murchie S, Erard S (1996) The spectral properties and composition of Phobos from measurements by Phobos 2. Icarus 123:63–86. https://doi.org/10.1006/icar.1996.0142

Murchie SL, Britt DT, Head JW, Pratt SF, Fisher PC, Zhukov BS, Kuzmin AA, Ksanfomality LV, Zharkov AV, Nikitin GE, Fanale FP, Blaney DL, Bell JF, Robinson MS (1991) Color heterogeneity of the surface of Phobos: relationships of geological features and comparison to meteorite analogs. J Geophys Res 96:5925–5945. https://doi.org/10.1029/90JB02354

Murchie S, Thomas N, Britt D, Herkenhoff K, Bell JF (1999) Mars pathfinder spectral measurements of Phobos and Deimos: comparison with previous data. J Geophys Res 104:9069–9079. https://doi.org/10.1029/98JE02248

Murchie SL, Thomas PC, Rivkin AS, Chabot NL (2015) Phobos and Deimos. In: Asteroids IV, Patrick Michel, Francesca E. DeMeo, and William F. Bottke (eds) University of Arizona Press, Tucson, 895 pp. ISBN: 978-0-816-53213-1, p.451–46

Murchie S, Choo T, Humm D, Rivkin AS, Bibring J-P, Langevin Y, Gondet B, Roush TL, Duxbury T, AND CRISM Team (2008) MRO/CRISM observations of Phobos and Deimos LPSC, 39: 1434

Nakamura T et al (2021) Science operation plan of Phobos and Deimos from the MMX spacecraft. Earth Planets Space. https://doi.org/10.1186/s40623-021-01546-6.

Ockert-Bell ME, Bell JF, Pollack JB, McKay CP, Forget F (1997) Absorption and scattering properties of the Martian dust in the solar wavelengths. J Geophys Res Planets 102(E4):9039–9050. https://doi.org/10.1029/96JE03991

Olsen KS, Forget F, Madeleine J-B, Szantai A, Audouard A, Geminale A, Altieri F, Bellucci G, Montabone L, Wolff MJ (2017) The distributions of retrieved properties from water ice clouds in the Martian atmosphere using the OMEGA imaging spectrometer. MAMO 2017 Conference proc. 3206

Pajola M, Lazzarin M, DalleOre CM, Cruikshank DP, Roush TL, Magrin S, Bertini I, La Forgia F, Barbieri C (2013) Phobos as a D-type captured asteroid, spectral modeling from 0.25 to 4.0 μm. Astrophys J 777:127. https://doi.org/10.1088/0004-637X/777/2/127

Pang KD, Pollack JB, Veverka J, Lane AL, Ajello JM (1978) The composition of Phobos—evidence for carbonaceous chondrite surface from spectral analysis. Science 199:64–66. https://doi.org/10.1126/science.199.4324.64

Pieters CM, Goswami JN, Clark RN, Annadurai M, Boardman J, Buratti B, Combe J-P, Dyar MD, Green R, Head JW, Hibbitts C, Hicks M, Isaacson P, Klima R, Kramer G, Kumar S, Livo E, Lundeen S, Malaret E, McCord T, Mustard J, Nettles J, Petro N, Runyon C, Staid M, Sunshine J, Taylor LA, Tompkins S, Varanasi P (2009) Character and spatial distribution of OH/H2O on the surface of the Moon seen by M^3 on Chandrayan-1. Science 326(5952):586–572. https://doi.org/10.1126/science.1178658

Pieters CM, Murchie S, Thomas N, Britt D (2014) Composition of surface materials on the Moons of Mars. Planet Space Sci 102:144–151. https://doi.org/10.1016/j.pss.2014.02.008

Pignatale FC, Charnoz S, Rosenblatt P, Hyodo R, Nakamura T, Genda H (2018) On the impact origin of Phobos and Deimos. III. Resulting composition from different impactors. Astrophys J 853(2). https://doi.org/10.3847/1538-4357/aaa23e

Pollack JB, Veverka J, Pang KD, Colburn DS, Lane AL, Ajello JM (1978) Multicolor observations of Phobos with the Viking lander cameras—evidence for a carbonaceous chondritic composition. Science 199:66–69. https://doi.org/10.1126/science.199.4324.66

Ramsley KR, Head JW (2013) Mars impact ejecta in the regolith of Phobos: bulk concentration and distribution. Planet Space Sci 87:115–129. https://doi.org/10.1016/j.pss.2013.09.005

Reuter DC, Simon AA, Hair J, Lunsford A, Manthripragada S, Bly V, Bos B, Brambora C, Caldwell E, Casto G, Dolch Z, Finneran P, Jennings D, Jhabvala M, Matson E, McLelland M, Roher W, Sullivan T, Weigle E, Wen Y, Wilson D, Lauretta DS (2018) The OSIRIS-REx visible and infrared spectrometer (OVIRS): spectral maps of the asteroid Bennu. Space Sci Rev 214:54. https://doi.org/10.1007/s11214-018-0482-9

Rivkin AS, Brown RH, Trilling DE, Bell JF III, Plassmann JH (2002) Near-infrared spectrophotometry of Phobos and Deimos. Icarus 156:64–75. https://doi.org/10.1006/icar.2001.6767

Rosenblatt P, Charnoz S (2012) On the formation of the martian moons from a circum-martian accretion disk. Icarus 221(2):806–815. https://doi.org/10.1016/j.icarus.2012.09.009

Rosenblatt P, Charnoz S, Dunseath KM, Terao-Dunseath M, Trinh A, Hyodo R, Genda H, Toupin S (2016) Accretion of Phobos and Deimos in an extended debris disc stirred by transient moons. Nat Geosci 9(8):581–583. https://doi.org/10.1038/ngeo2742

Rosenqvist J, Drossart P, Combes M, Encrenaz T, Lellouch E, Bibring JP, Erard S, Langevin Y, Chassefiere E (1992) Minor constituents in the Martian atmosphere from the ISM/Phobos experiment. Icarus 98(2):254–270. https://doi.org/10.1016/0019-1035(92)90094-N

Roush TL, Singer RB (1987) Possible temperature variation effects on the interpretation of Spatially Resolved Reflectance observations of asteroid surfaces. Icarus 69:571. https://doi.org/10.1016/0019-1035(87)90026-1

Ryan AJ, Pino Muñoz D, Bernacki M, Delbo M (2020) Full-field modeling of heat transfer in asteroid regolith: radiative thermal conductivity of polydisperse particulates. J Geophys Res 125:e06100. https://doi.org/10.1029/2019JE006100

Sakatani N, Ogawa K, Iijima Y, Arakawa M, Honda R, Tanaka S (2017) Thermal conductivity model for powdered materials under vacuum based on experimental studies. AIP Adv 7:015310. https://doi.org/10.1063/1.4975153

Sasaki S (1990) Origin of Phobos—aerodynamic drag capture by the primary atmosphere of Mars. Lunar Planet Sci XXI:1069–1070 (abstract)

Simonelli DP, Wisz M, Switala A, Adinolfi D, Veverka J, Thomas PC, Helfenstein P (1998) Photometric properties of Phobos surface materials from Viking images. Icarus 131:52–77. https://doi.org/10.1006/icar.1997.5800

Singer RB, Rouch TL (1985) Effects of temperature on remotely sensed Mineral absorption features. JGR 90:12434. https://doi.org/10.1029/JB090iB14p12434

Smith BA (1970) Phobos: preliminary results from Mariner 7. Science 168:828

Smith MD, Wolff MJ, Clancy RT, Murchie SL (2009) Compact reconnaissance imaging spectrometer observations of water vapor and carbon monoxide. J Geophys Res 114:E00D03. https://doi.org/10.1029/2008JE003288

Smith MD, Wolff MJ, Clancy RT, Kleinboehl A, Murchie SL (2013) Vertical distribution of dust and water ice aerosols from CRISM limb-geometry observations. J Geophys Res Planets 118(2):321–334. https://doi.org/10.1002/jgre.20047

Smith NM, Edwards CS, Mommert M, Trilling DE, Glotch TD (2019) MGS-TES Spectra of Phobos indicate Thermally Homogeneous surface. LPICo2089.6391S

Spencer JR, Lebofsky LA, Sykes MV (1989) Systematic biases in radiometric diameter determinations. Icarus 78:337–354. https://doi.org/10.1016/0019-1035(89)90182-6

Spiga A, Faure J, Madeleine J-B, Määttänen A, Forget F (2013) Rocket dust storms and detached dust layers in the Martian atmosphere. JGRE 118:746. https://doi.org/10.1002/jgre.20046

Spiga A, González-Galindo F, López-Valverde M-Á, Forget F (2012) Gravity waves, cold pockets and CO_2 clouds in the Martian mesosphere. Geo RL 39: 2201. https://doi.org/10.1002/jgre.20046

Szeto AMK (1983) Orbital evolution and origin of the Martian satellites. Icarus 55:133–168. https://doi.org/10.1016/0019-1035(83)90056-8

Thomas PC, Veverka J, Bloom A, Duxbury TC (1979) Grooves on Phobos: their distribution, morphology, and possible origin. J Geophys Res 84:8457–8477. https://doi.org/10.1029/JB084iB14p08457

Thomas PC, Adinolfi D, Helfenstein P, Simonelli D, Veverka J (1996) The surface of Deimos: contribution of materials and processes to its unique appearance. Icarus 123:536–556. https://doi.org/10.1006/icar.1996.0177

Thomas N, Stelter R, Ivanov A, Bridges NT, Herkenhoff KE, McEwen AS (2011) Spectral heterogeneity on Phobos and Deimos: HiRISE observations and comparisons to Mars Pathfinder results. Planet Space Sci 59:1281–1292. https://doi.org/10.1016/j.pss.2010.04.018

Touma J, Wisdom J (1993) The chaotic obliquity of Mars. Science 259(5099):1294–1297. https://doi.org/10.1126/science.259.5099.1294

Vincendon M, Langevin Y, Poulet F, Pommerol A, Wolff M, Bibring JP, Gondet B, Jouglet D (2009) Yearly and seasonal variations of low albedo surfaces on Mars in the OMEGA/MEx dataset: Constraints on aerosols

properties and dust deposits. Icarus 200(2):395–405. https://doi.org/10.1016/j.icarus.2008.12.012
Vincendon M, Langevin Y, Poulet F, Bibring JP, Gondet B (2007) Recovery of surface reflectance spectra and evaluation of the optical depth of aerosols in the near-IR using a Monte Carlo approach: application to the OMEGA observations of high-latitude regions of Mars. J Geophys Res Planets 112(E8). https://doi.org/10.1029/2006JE002845
Vincendon M, Pilorget C, Gondet B, Murchie S, Bibring J-P (2011) New near-IR observations of mesospheric CO_2 and H_2O clouds on Mars. J Geophys Res E Planets 116: 0–02. https://doi.org/10.1029/2011JE003827
Wiens RC, Maurice S, Robinson SH, Nelson AE, Caïs P et al (2021) The SuperCam Instrument Suite on the NASA Mars 2020 Rover: Body Unit and Combined System Tests. Space Sci Rev 217:4. https://doi.org/10.1007/s11214-020-00777-5
Willner K, Shi X, Oberst J (2014) Phobos' shape and topography models. Planet Space Sci 102:52–59. https://doi.org/10.1016/j.pss.2013.12.006
Zellner B, Wells EN (1994) Spectrophotometry of Martian satellites with the Hubble Space Telescope. Lunar Planet Sci Conf 25:1541–1542

Publisher's Note